Available online at www.sciencedirect.com
ScienceDirect
Journal of Power Sources 165 (2007) 517–534
JOURNAL OF POWER SOURCES
www.elsevier.com/locate/jpowsour

Structural and electrochemical behavior of $LiMn_{0.4}Ni_{0.4}Co_{0.2}O_2$

Miaomiao Ma[a,1], Natasha A. Chernova[a], Brian H. Toby[b,2], Peter Y. Zavalij[a,3], M. Stanley Whittingham[a,*]

[a] *Institute for Materials Research, State University of New York at Binghamton, Binghamton, NY 13902, USA*
[b] *NIST Center for Neutron Research, National Institute of Standards and Technology, Gaithersburg, MD 20899, USA*

Available online 17 November 2006

Abstract

Layered $LiMn_{0.4}Ni_{0.4}Co_{0.2}O_2$ with the α-$NaFeO_2$ structure was synthesized by the "mixed hydroxide" method, followed by a high temperature calcination at 800 °C giving a single phase material of surface area 5 $m^2\,g^{-1}$. A combined X-ray/neutron diffraction Rietveld refinement showed that the transition metals in the 3b layer are randomly distributed at room temperature, and that only nickel migrates to the lithium layer and in this case 4.4%. Addition of excess lithium reduces the amount of nickel on the lithium sites. The magnetic susceptibilities of the compounds $LiMn_yNi_yCo_{1-2y}O_2$ ($y = 0.5$, 0.4, 0.333) follow the Curie–Weiss law above 100 K and are consistent with the presence of Ni^{2+}, Mn^{4+} and Co^{3+} cations; their magnetization curves, measured at 5 K and showing a pronounced hysteresis, are also consistent with the nickel content on the lithium sites increasing with decreasing cobalt content. This material shows a stable capacity of 140–170 mA h g^{-1} for more than 90 cycles within the voltage window of 2.5–4.4 V. The layered rhombohedral structure is maintained as lithium is removed down to at least a lithium content of 0.05; the total volume change on cycling is under 2%. The nickel ions pin the lattice so that MO_2 slab sliding to form the 1T structure cannot readily occur. The capability of aqueous acids to leach lithium from the lattice decreases with increasing nickel content in the lithium layer; however, the thermal stability of the delithiated compounds increases with cobalt content.
© 2006 Elsevier B.V. All rights reserved.

Keywords: Neutron diffraction; Lithium battery; Rietveld analysis; Magnetism; Ordering

1. Introduction

Layered materials have been extensively studied as the cathode of lithium batteries since the original work on TiS_2 [1,2] and $LiCoO_2$ [3,4]. The latter dominates the present commercial lithium batteries [5], but the scarcity of cobalt ores in nature results in a high price that will restrict its use in large-scale batteries such as might be used in hybrid electric vehicles. $LiNiO_2$ is iso-structural with $LiCoO_2$ but cannot be used in the pure state because of the high oxygen partial pressure at low lithium contents. It has been stabilized by the addition of some cobalt and by the incorporation of some trivalent ions such as aluminum, which prevents the total removal of all of the lithium [6]. Nickel and cobalt form a complete solid solution for $0 \le y \le 1$ in $LiNi_yCo_{1-y}O_2$ [7–9]. There has been much interest in the lower cost manganese oxides, which exist in many structural forms with the alkali metals. However, $LiMnO_2$ cannot be formed with the $R\bar{3}m$ structure under normal reaction conditions, because it is unstable at the high temperatures used. It can be synthesized hydrothermally followed by lithium intercalation, or by the ion exchange of the sodium analog $NaMnO_2$ [10,11], as may also the mixed compound $LiMn_yCo_{1-y}O_2$ [12–14]. $LiNiO_2$ and $LiMnO_2$ also form a solid solution up to 50% manganese [15,16]. It was recognized [17–20] that based on the binary mixed metal oxides, that the ternary $LiMn_yNi_qCo_{1-y-q}O_2$ ought to exist. The breadth of the $LiMn_yNi_qCo_{1-y-q}O_2$ solid solution is presented in Fig. 1; the solid solution can be extended toward higher manganese contents using soft synthesis approaches as described above. The solid points represent the known compounds synthesized with the $R\bar{3}m$ structure [16–32]. Much effort has been focused on the compounds containing equal amounts of Ni and Mn, $LiMn_yNi_yCo_{1-2y}O_2$, (center line perpendicular to the Ni side), and on compounds containing less Co with the goal of finding the optimum electrochemical

* Corresponding author. Tel.: +1 607 777 4623; fax: +1 607 777 4623.
E-mail address: stanwhit@gmail.com (M.S. Whittingham).
[1] Present address: Johnson Controls Inc., 5757 North Green Bay Avenue B-67, Milwaukee, WI 53209, USA.
[2] Present address: Advanced photon Source, Argonne National Laboratory, Argonne, IL 60439, USA.
[3] Present address: Chemistry Department, University of Maryland, College Park, MD, USA.

0378-7753/$ – see front matter © 2006 Elsevier B.V. All rights reserved.
doi:10.1016/j.jpowsour.2006.10.022

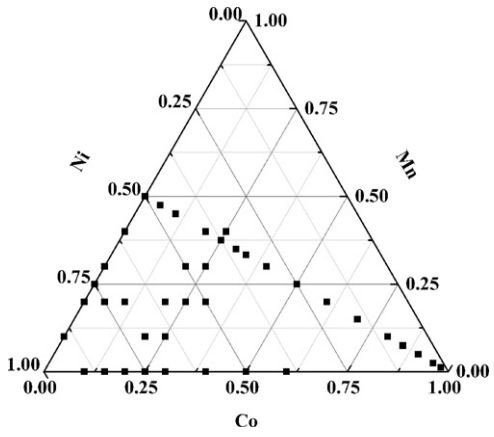

Fig. 1. Composition diagram of the $LiMn_yNi_qCo_{1-q-y}O_2$ solid solution.

composition combined with high stability and low cost [33]. Among these compounds, most research has emphasized either $LiNi_{0.5}Mn_{0.5}O_2$ [16,21–23] or $LiMn_{1/3}Ni_{1/3}Co_{1/3}O_2$ with equal amount of the three metals [19,29,34–37]. The presence of cobalt plays a critical role in minimizing the transition metal content in the lithium layer, and perhaps also in enhancing the electronic conductivity; however, it is in limited supply and therefore more costly than nickel or manganese. Here, we present a study of an intermediate cobalt content compound $LiMn_{0.4}Ni_{0.4}Co_{0.2}O_2$.

2. Experimental

The $LiMn_yNi_yCo_{1-2y}O_2$ ($y = 1/3$, 0.4, 0.5) compounds were synthesized by the mixed hydroxide method [17], followed by high temperature solid-state heating as in our previous work [27]. Stoichiometric amounts of $Mn(OAc)_2{\cdot}4H_2O$ (99+%, Aldrich), $Ni(NO_3)_2{\cdot}6H_2O$ (98%, Aldrich), and $Co(OAc)_2{\cdot}4H_2O$ (Aldrich) were dissolved in distilled water and dripped into a $LiOH{\cdot}H_2O$ (98+%, Aldrich) solution with three times the molar amount of the sum of the metal salts. The precipitates of $Mn_yNi_yCo_{1-2y}(OH)_2{\cdot}nH_2O$ were filtered and washed thoroughly with distilled water; they were dried overnite at 60–70 °C. The resulting powder was mixed with 1.05 moles of $LiOH{\cdot}H_2O$, made into pellets and heated first at 450 °C for 12 h and then at 800 °C for 8 h. The samples were ground and repelletized between the two heatings, and then removed from the oven giving a rapid cooling.

The electrochemical properties of the $LiMn_{0.4}Ni_{0.4}Co_{0.2}O_2$ were examined using both bag cells and coin cells containing pure lithium as the anode at room temperature in a helium filled glove box. The bag cell cathodes were made by mixing 80 wt.% of the oxide with 10 wt.% of acetylene black and 10 wt.% of Teflon™ as the binder, and pressing into a stainless Exmet™ screen at 5 tonnes pressure and 180 °C for 2 h. The coin cell cathode paste was made by mixing 80 wt.% of $LiMn_{0.4}Ni_{0.4}Co_{0.2}O_2$ with 10 wt.% of PVDF [poly(vinylidene fluoride)], and 10 wt.% of acetylene black in NMP (1-methyl-2-pyrrolidinone). The paste was laminated on aluminum foil and vacuum dried at 70 °C before use. The electrolyte was 1 M $LiPF_6$ (lithium hexafluorophosphate) dissolved in a 1:1 volume ratio solution of EC (ethylene carbonate) and DMC (dimethyl carbonate) (Merck). Cells were cycled galvanostatically using a MacPile II cycler, or a VMP2 Multi-potentiostat (Princeton Applied Research).

X-ray powder diffraction data were collected on a Scintag XDS2000 θ–θ powder diffractometer equipped with a Ge(Li) solid state detector and Cu Kα sealed tube ($\lambda = 1.54178$ Å). Data were measured over the range of 15–90° 2θ with a step size of 0.02° and exposure of 5 s for routine characterization and over the range of 15–120° 2θ with a step size of 0.02° and exposure of 10 s for structure refinement; the samples were rotated. Neutron powder diffraction data were collected using the BT-1 32 detector neutron powder diffractometer at the NIST Center for Neutron Research, NBSR. A Cu (3 1 1) monochromator with a 90° take-off angle, $\lambda = 1.5402(2)$ Å, and in-pile collimation of 15 min of arc were used. Data were collected over the range of 3–168° 2θ with a step size of 0.05°. The sample was loaded in a vanadium can sample container of length 50 mm and diameter 6 mm. Data were collected under ambient conditions. The Rietveld refinement used both the individual and combined X-ray and neutron powder diffraction patterns using the GSAS/EXPGUI package [38,39].

Chemical analysis of the samples were done by Direct Current Plasma spectroscopy (ARL SS-7). Scanning electron microscopy images were obtained using an Electron Scan instrument at a magnification of 5000× and 25,000×. Thermogravimetric analysis (TGA) was carried out with a TA Instruments 2950, with a 5 °C min^{-1} heating rate under nitrogen. The specific surface area of the $LiMn_{0.4}Ni_{0.4}Co_{0.2}O_2$ was determined by nitrogen absorption experiment using the BET method at 77 K with a Micromeritics ASAP2020 Surface Area Porosity Analyzer. The magnetic measurements were performed using a SQUID magnetometer (Quantum Design MPMS XL-5). The temperature dependences of the magnetic susceptibility were obtained from 298 to 2 K in a magnetic field of 0.1 T. The magnetization curves were measured at 5 K in magnetic fields up to 5 T. Samples with reduced lithium content were obtained electrochemically by coulometric titration at a rate of 0.1 mA cm^{-2} followed by a 10 h relaxation. These samples were then X-rayed after electrolyte removal by drying with a tissue. The acid leaching was conducted by mixing 1.2 molar CH_3COOH, H_3PO_4, HF, HCl, or H_2SO_4, with the active material $LiMn_yNi_yCo_{1-2y}O_2$ ($y = 0.33$, 0.4, 0.5) in the ratio of $H^+/LiMO_2 = 5{:}1$. The mixtures were stirred at room temperature for 5 h, filtered, washed with acetone, and dried at 100 °C.

3. Results and discussion

3.1. Chemical analysis

Chemical analysis of the "$LiMn_{0.4}Ni_{0.4}Co_{0.2}O_2$" synthesized at 800 °C indicated essentially the perfect composition, $Li_{1.0}Mn_{0.40}Ni_{0.40}Co_{0.20}O_2$, when 5% excess lithium is used in the reaction; using the stoichiometric amount of lithium in the reaction medium resulted in a final lithium content around 0.95. Fig. 2 shows the scanning electron microscopy (SEM) image of this material. The particles are uniform in size and under 1 μm; they have defined edges in agreement with the high crystallinity

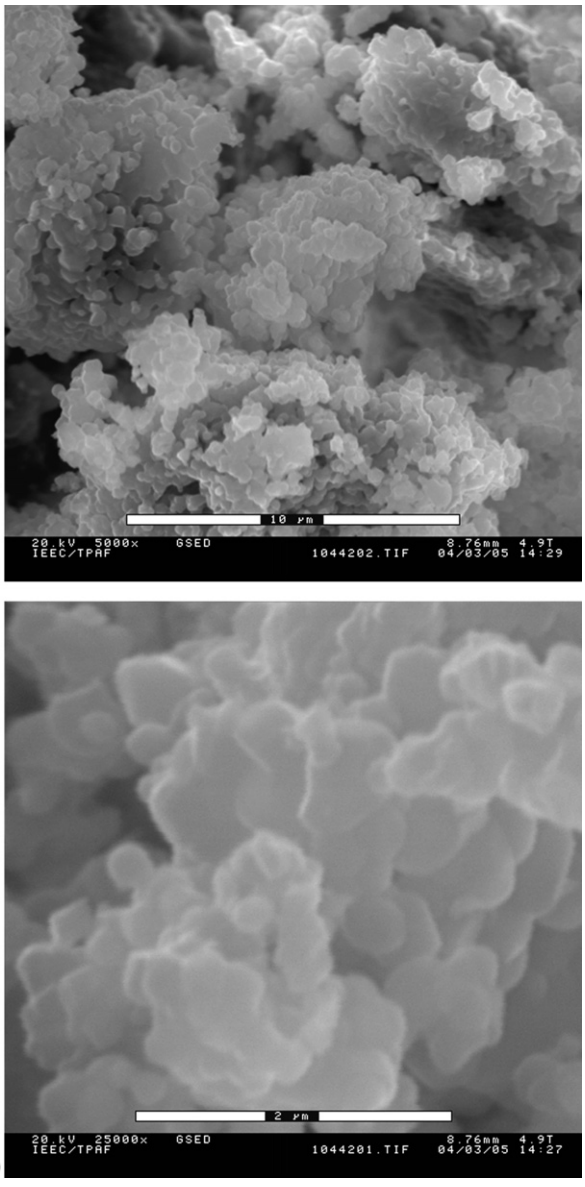

Fig. 2. SEM images of $LiMn_{0.4}Ni_{0.4}Co_{0.2}O_2$ at a magnification of (a) 5000× and (b) 25,000×.

resulting from the high temperature heating, which was also indicated by the sharper X-ray diffraction reflections. The BET surface area of $LiMn_{0.4}Ni_{0.4}Co_{0.2}O_2$ was found to be 5.14 $m^2\,g^{-1}$, which based on the XRD density of 4.725 $g\,cm^{-3}$ (Table 1) is consistent with plate-like particles 0.5 μm on a side and 0.12 μm thick as observed in Fig. 2(b). Extended mechanical grinding gave hardly any increase in the surface area, thus the surface area and particle size are primarily determined by the synthesis temperature. This surface area is higher than that reported for $Li_{1+z}(Mn_{1/3}Ni_{1/3}Co_{1/3})_{1-z}O_2$ synthesized at 900 °C, which ranged from 0.4 to 0.8 $m^2\,g^{-1}$ [40]. The optimum surface area will depend on the application, and the desired safety margins; high rate applications will require either higher lithium diffusion coefficients or higher surface areas [41]. However, lower surface areas minimize side-reactions with the electrolyte, improve the thermal stability [42] and enhance the safety of the system, but are likely to lead to lower power capabilities. In addition, they minimize the amount of SEI needed and the dissolution of the oxide into the electrolyte [43].

3.2. Thermogravimetric analyses of transition metal hydroxides and the layered compound $LiMn_{0.4}Ni_{0.4}Co_{0.2}O_2$

The thermal stabilities of the hydroxide precursors and of the oxide itself were determined, and are shown in Fig. 3. The coprecipitates $Mn_{0.4}Ni_{0.4}Co_{0.2}(OH)_2$ and $Mn_{1/3}Ni_{1/3}Co_{1/3}(OH)_2$ lose 21.28 and 19.76 wt.%, respectively, upon heating in nitrogen with water loss and transition metal oxide formation. The weight loss, besides that due to surface water (about 5 wt.%), is close to the formation of M_3O_4 [44], where M = Mn + Ni + Co. We found that the protons could also be removed in an electrochemical cell forming the oxide MO_2, where M = Mn + Ni + Co, in a similar manner to the formation of ε-$VOPO_4$ from $VPO_4.H_2O$ [45]; this work will be published elsewhere. Fig. 3(b) shows the weight loss of $LiMn_{0.4}Ni_{0.4}Co_{0.2}O_2$ when heated in nitrogen at a rate of 5 °C min^{-1} up to 600 °C. The weight loss of $LiMn_{0.4}Ni_{0.4}Co_{0.2}O_2$ was less than 0.05%, showing the excellent thermal stability of the fully lithiated compound; and the absence of any surface impurities like hydroxide or carbonate. For a pure layered lithium transition metal oxide, any deficit of lithium would have led to a reduction of some transition metal and oxygen loss [46] as will be discussed later in this paper.

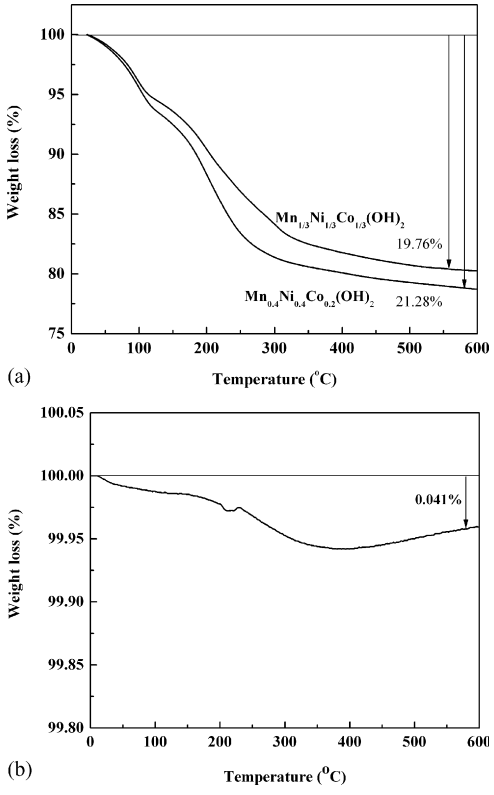

Fig. 3. Thermogravimetric analyses of (a) $Mn_{0.4}Ni_{0.4}Co_{0.2}(OH)_2$, $Mn_{1/3}Ni_{1/3}Co_{1/3}(OH)_2$ and (b) $LiMn_{0.4}Ni_{0.4}Co_{0.2}O_2$ in nitrogen at a heating rate of 5 °C min^{-1} to 600 °C.

3.3. Structure and nickel disorder in $LiMn_{0.4}Ni_{0.4}Co_{0.2}O_2$

The $LiMn_{0.4}Ni_{0.4}Co_{0.2}O_2$ compound crystallizes in the trigonal system (space group $R\bar{3}m$) that belongs to the α-$NaFeO_2$ structure type shown in Fig. 4. Some transition metal is invariably found in the lithium layer (3a site) displacing that lithium to the transition metal layer (3b site). These transition metal ions pin the MO_2 oxide blocks, potentially reducing the electrochemical capacity and the ultimate rate capability; they may also play a key positive role in preventing structural change and chemical reactivity. A full Rietveld refinement of the X-ray diffraction pattern of $LiMn_{0.4}Ni_{0.4}Co_{0.2}O_2$ compound was performed to determine the degree of cation mixing. The resulting data are shown in Table 1 and Fig. 4(a). The $c/3a$ ratio of 1.658 shows a high-layered character [27], and the Rietveld refinement indicates 4.4(1) at.% transition metal content in the Li layer. However, the X-ray powder data cannot differentiate between the Mn, Ni and Co because they have similar X-ray scattering factors, nor can we be certain from the X-ray analysis of the lithium content in the transition metal layer because of its low scattering factor except through a chemical analysis. A complete chemical analysis indicated the following chemical composition for this sample: $Li_{1.0}Mn_{0.40}Ni_{0.40}Co_{0.20}O_2$. Thus, we can safely

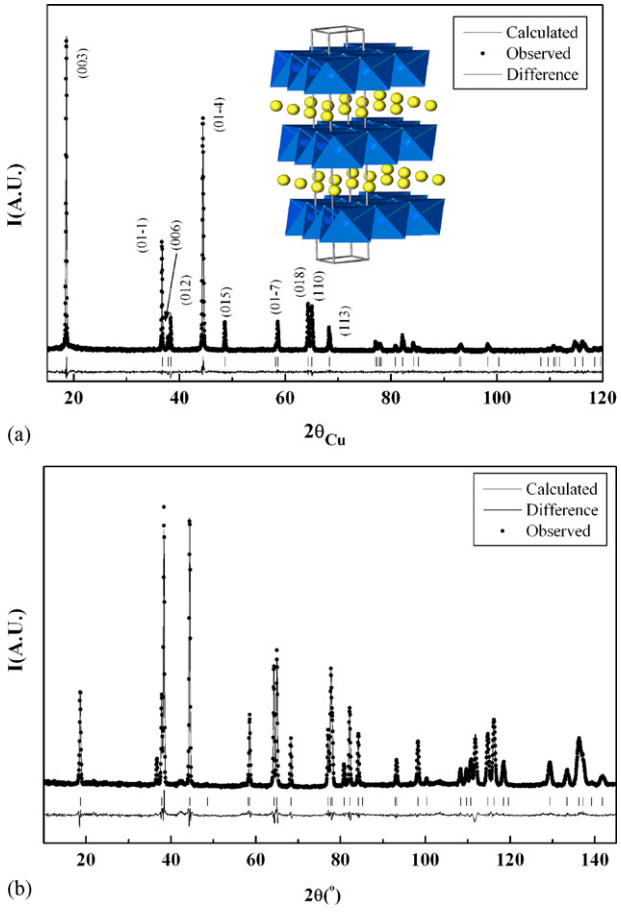

Fig. 4. Rietveld refinement of (a) X-ray (the α-$NaFeO_2$-type structure ($R\bar{3}m$) of $LiMn_{0.4}Ni_{0.4}Co_{0.2}O_2$ are shown in the center; the lithium and transition metals are in the centers of edge-sharing octahedra) and (b) neutron diffraction patterns for $LiMn_{0.4}Ni_{0.4}Co_{0.2}O_2$. The position of the lines and the difference plot are shown below the patterns.

Table 1
Crystal data, experimental and refinement details for $LiMn_{0.4}Ni_{0.4}Co_{0.2}O_2$

Crystal data		
Chemical formula	$(Li_{1-x}Ni_x)(Mn_{0.4}Ni_{0.4-x}Li_xCo_{0.2})O_2$, $x = 0.0438(7)$	
M_r (a.m.u.)	96.18	
Cell setting	Trigonal	
Space group	$R\bar{3}m$	
a (Å)	2.86616(2)	
c (Å)	14.2542(2)	
V (Å^3)	101.408(2)	
Z	3	
D_x (g cm^{-3})	4.725	
Temperature (K)	298	
Diffractometer	**Scintag XDS2000**	**BT-1 32**
Experimental details		
Radiation	Cu Kα	Neutrons
Wavelength (Å)	1.54178	1.53992(2)
Data collection method	Step scan	Step scan
2θ range (°)	15–120	3–168
2θ step size (°)	0.02	0.05
Exposure/step (s)	10	–
Refinement details		
Method	Full profile (Rietveld)	
Number of reflections	32	39
R_{prof}[a]	0.0321	0.0333
wR_{prof}[a]	0.0408	0.0408
R_{exp}[a]	0.0355	0.0302
R_{Bragg}[a]	0.0431	0.0473

[a] $R_{prof} = \sum_{i=1}^{n} |Y_i^{obs} - Y_i^{calc}| / \sum_{i=1}^{n} Y_i^{obs}$;

$wR_{prof} = \left[\sum_{i=1}^{n} w_i (Y_i^{obs} - Y_i^{calc})^2 / \sum_{i=1}^{n} w_i (Y_i^{obs})^2 \right]^{1/2}$;

$R_{exp} = \left[(n-p) / \sum_{i=1}^{n} w_i (Y_i^{obs})^2 \right]^{1/2}$;

$R_{Bragg} = \sum_{i=1}^{n} |F_i^{2\,obs} - F_i^{2\,calc}| / \sum_{i=1}^{n} F_i^{2\,obs}$.

make the assumption that there is one cation in the lithium layer and one cation in the transition metal layer, so that the layer composition must be $Li_{0.96}M_{0.04}[Li_{0.04}M_{0.96}]O_2$, where M is at least one of Mn, Ni, and Co.

In contrast to X-ray scattering, the neutron scattering factors for Mn, Ni, and Co are very different (Mn −0.373, Co 0.249, Ni 1.03, and Li −0.190). Therefore, the neutron powder diffraction pattern was collected and used in a combined Rietveld refinement with the X-ray data. Despite the substantial difference in the neutron scattering factors, the presence of four (including Li) metals that can occupy the same site can make the determination of the metal distribution hard or even impossible, for example, a mixture of 55% of Mn and 45% of Ni will show the same neutron scattering as 100% of Co. However, the X-ray data, showing that 4.4(1)% transition metal interchanges with Li, agrees with the neutron data only if this transition metal has the highest neutron scattering factor, which is Ni. Absence of additional diffraction peaks in the neutron powder pattern shows that there is no long-range ordering in the distribution of the transition metals and they randomly occupy the 3b site except for the small fraction of Ni exchanged with Li from 3a site. In the final structural refinement the occupation factors of Mn and Co were set to 0.4 and 0.2, respectively, and not refined. The total content of Li and Ni were set as 1 and 0.4, respec-

Table 2
Atomic parameters and constrains for $LiMn_{0.4}Ni_{0.4}Co_{0.2}O_2$

Atoms	Site	x, y, z	Occupation (G)[a]
Li1, Ni1	3a	0, 0, 0	0.9562(7)Li + 0.0438(7)Ni[b]
Mn2, Co2, Ni2, Li2	3b	0, 0, 1/2	0.4Mn + 0.2Co + 0.3562(7)Ni + 0.0438(7)Li
O	6c	0, 0, 0.24147(3)[b]	

[a] Constrains: $G_{Ni1} = G_{Li2} = 1 - G_{Li1} = 0.4 - G_{Ni2}$; $G_{Mn2} = 0.4$; $G_{Co2} = 0.2$; $G_{Ni1} + G_{Ni2} = 1 - G_{Mn2} - G_{Co2} = 0.4$.
[b] Refined parameter.

tively, but their distribution between 3a (Li1, Ni1) and 3b (Li2, Ni2) sites was refined so that $G_{Li1} + G_{Ni1} = 1$, $G_{Li2} + G_{Ni2} = 0.4$ and $G_{Li1} + G_{Li2} = 1$, $G_{Ni1} + G_{Ni2} = 0.4$. The only refined coordinate was z of oxygen atoms residing in the 6c site (0, 0, z). The combined Rietveld refinement using X-ray and neutron shows good agreement as can be seen from Table 1 and Fig. 4. The final atomic coordinates and distribution of transition metals and Li are shown in Table 2. Thus, the final composition is $(Li_{0.956},Ni_{0.044})(Mn_{0.4},Ni_{0.356},Li_{0.044},Co_{0.2})O_2$, which corresponds to the total composition $Li(Mn_{0.4},Ni_{0.4},Co_{0.2})O_2$ with 0.0438(7) Li exchanged for Ni. The resulting bond distances are: for the metal in the 3a site δ(Li1–O) is 2.1102(6) Å and for 3b site δ(Mn2–O) is 1.9686(2) Å. Both sites have slightly distorted octahedral coordination with O–Li1–O angles of 85.55(1)° and 94.45(1)° and O–Mn2–O angles of 86.56(1)° and 93.44(1)°.

3.4. The impact of excess lithium on the structure

In the last few years there has been an increasing interest in materials containing excess lithium, $Li(Li_zM_{1-z})O_2$, where M is at least one element selected from Mn, Ni, and Co. Studies by Zhang et al. [47] and Shin et al. [48] showed that though the average oxidation state of the transition metals increases, which means the amount of the electrochemically active transition metal decreases, to compensate the increasing amount of lithium, Li–Mn–Ni–O compounds with excess lithium delivered much higher capacity than that of the stoichiometric $LiMn_{0.5}Ni_{0.5}O_2$ due probably to the achievement of structural stabilization by solid solution formation between $LiMn_{0.5}Ni_{0.5}O_2$ and Li_2MnO_3, in which Mn ions are tetravalent and cannot be easily oxidized. Here we explored structural changes and the effect on cation ordering when the lithium amount in the layered $Li_{1+z}[Mn_{0.4}Ni_{0.4}Co_{0.2}]_{1-z}O_2$ compound varies.

Due to the increasing amount of lithium in the layered compound $Li_{1+z}[Mn_{0.4}Ni_{0.4}Co_{0.2}]_{1-z}O_2$, the average oxidation state of the transition metals has to increase to balance the whole chemical formula. This increase could be provided by either the oxidation of Ni^{2+} to Ni^{3+}, or Co^{3+} to Co^{4+}. Our magnetic studies, discussed later, are consistent with the former and in agreement with the proposal of Tran et al. [49]. If we assume that all the Ni^{2+} is replaced by Ni^{3+}, then the maximum lithium content is $z = 1.167$ in $Li_{1+z}(Mn_{0.4}{}^{4+}Ni_{0.4}{}^{3+}Co_{0.2}{}^{3+})_{2-z}O_2$, without the formation of a second phase such as Li_2MnO_3.

$Li_{1+z}[Mn_{0.4}Ni_{0.4}Co_{0.2}]_{1-z}O_2$ oxides with different Li/M molar ratios x ($M = Mn_{0.4}Ni_{0.4}Co_{0.2}$, $0.9 < 1 + z < 1.25$) were synthesized by varying the mixed Li/M molar ratios after the mixed hydroxides were obtained. The nominal Li/M molar ratios and actual values from chemical analyses are listed in Table 3, where $M = Mn_{0.402}Ni_{0.395}Co_{0.203}$ from the DCP measurement. The morphologies of all samples were characterized by SEM and are shown in Fig. 5. The particle size decreased as the molar ratio of Li/M increased resulting in higher surface areas for the compounds with more lithium. This is contrary to what might be expected, with excess lithium impeding the sintering of the particles, and might signify the formation of an intergrowth of two phases. X-ray diffraction showed (Fig. 6(a)) that the extra lithium was incorporated into a "single-phase" compound of space group $R\bar{3}m$. The larger particle size observed in the SEM images for the lower value Li/M ratio was also reflected in a greater crystallinity in the XRD pattern. The diffraction patterns of the excess-lithium compounds shift toward higher angles compared to the lithium deficient and stoichiometric compounds, as can be seen clearly in the enlargement of the XRD patterns of Fig. 6(b), showing that the unit cell decreases with increasing lithium. The cell parameters and degree of cation disorder, obtained from the Rietveld refinement, are listed in Table 3. This unit cell size decrease may be associated with both the smaller ionic radius of the nickel ions due to their average increased oxidation state, and possibly because of the reduced cation mixing. Table 3 shows that the $c/3a$ ratio increases as the amount of lithium increases in $Li_{1+z}(Mn_{0.4}Ni_{0.4}Co_{0.2})_{1-z}O_2$, indicating increased deviation from the value of 1.633 and a more layered-like lattice [27]. The electrochemical behavior of the excess lithium

Table 3
Measured lithium content from DCP, and cell parameters and cation mixing from the Rietveld refinement of $Li_{1+z}[Mn_{0.4}Ni_{0.4}Co_{0.2}]_{1-z}O_2$ ($0.9 < 1 + z < 1.25$)

Initial ratio of Li/M	a	c	$c/3a$	Measured Li/M ratio from DCP	Occupancy of Ni on Li-site from GSAS refinement (%)
0.90	2.874	14.280	1.656	0.884	4.50
0.97	2.870	14.265	1.657	0.932	4.59
1.04	2.865	14.245	1.657	1.026	4.14
1.11	2.861	14.238	1.659	1.111	3.78
1.18	2.857	14.225	1.659	1.193	2.29
1.25	2.854	14.211	1.660	1.256	0.96

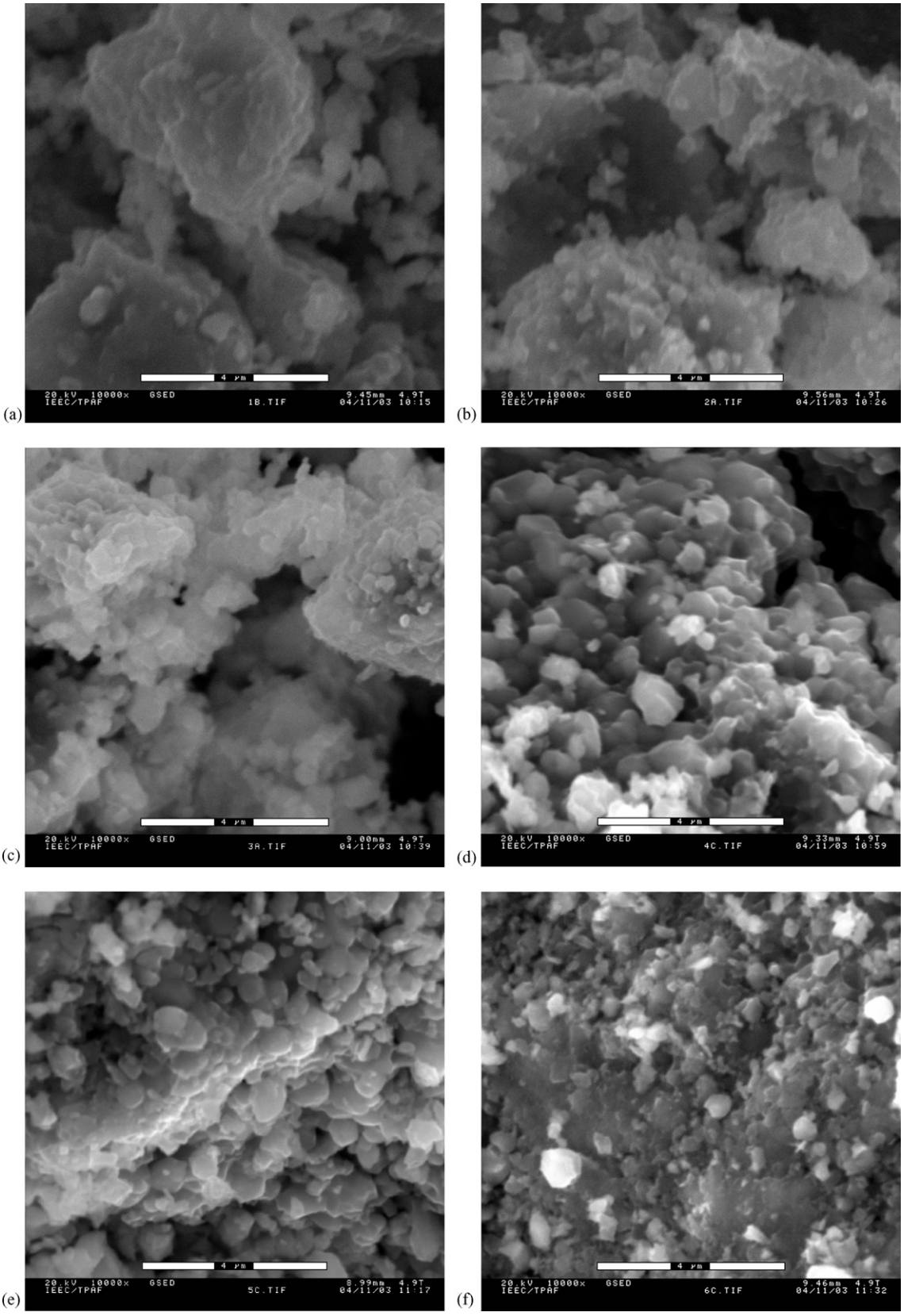

Fig. 5. SEM images of $Li_{1+z}[Mn_{0.4}Ni_{0.4}Co_{0.2}]_{1-z}O_2$ mixed oxides with different Li/metal ratios: (a) $1+z=0.9$; (b) $1+z=0.97$; (c) $1+z=1.04$: (d) $1+z=1.11$; (e) $1+z=1.18$; (f) $1+z=1.25$.

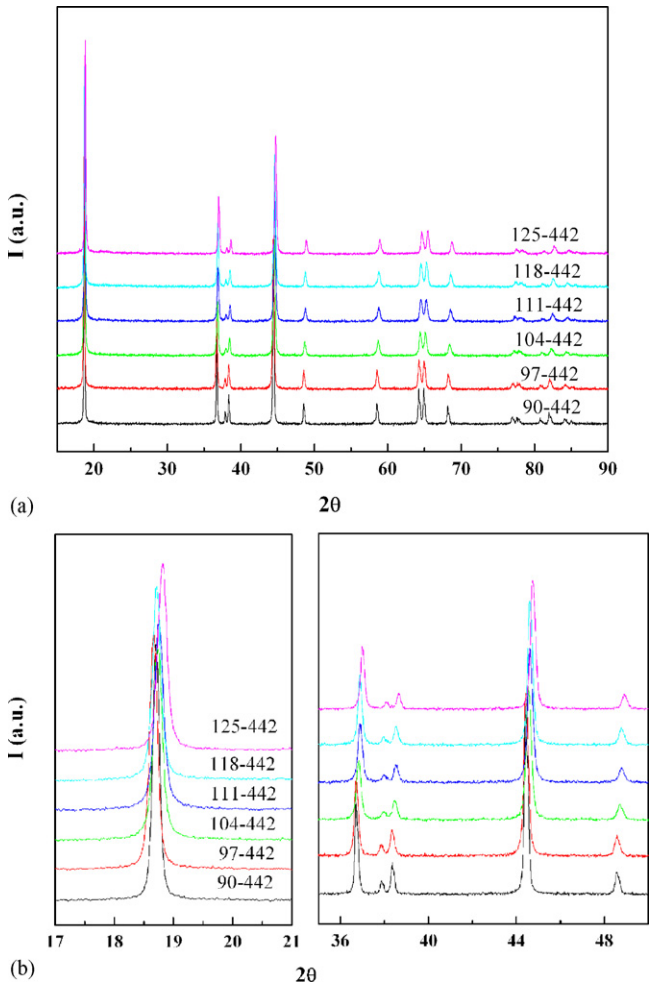

Fig. 6. (a) XRD patterns of $Li_z(Mn_{0.4}Ni_{0.4}Co_{0.2})_{1-z}O_2$ with different Li/M ratios (M = $Mn_{0.4}Ni_{0.4}Co_{0.2}$, $0.9 < z < 1.25$). (b) Enlargements of the (0 0 3) and (0 0 6)/(0 1 2) reflections. The composition of the samples are given in the format, 100–442, where the first number represents the Li/M ratio × 100 and the second number the ratio of the transition metals; for 100–442 this is $LiMn_{0.4}Ni_{0.4}Co_{0.2}O_2$.

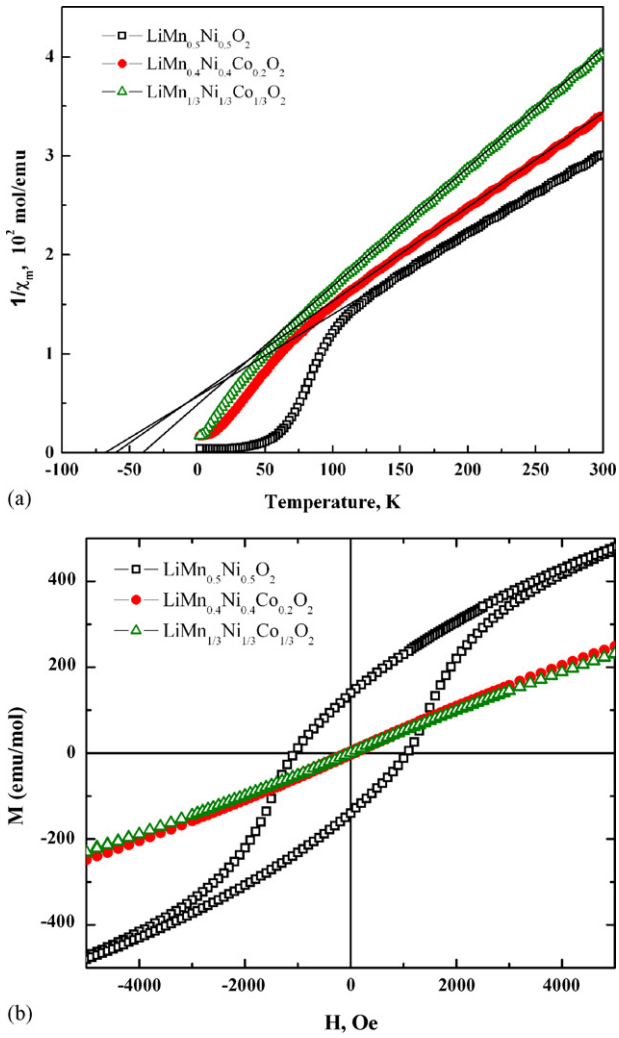

Fig. 7. Magnetic behavior of $LiMn_yNi_yCo_{1-2y}O_2$ ($y = 0.5, 0.4, 0.33$): (a) reciprocal magnetic susceptibility and its fit to the Curie–Weiss law (straight lines) at high temperatures, and (b) magnetization curves measured at 5 K.

layered compounds is of great interest since recent work suggests excess lithium on the layered $LiMn_{0.5}Ni_{0.5}O_2$ [50] and $LiMn_{1/3}Ni_{1/3}Co_{1/3}O_2$ [40,51,52] may give rise to an enhanced structural stability, resulting in high capacity, good cyclability, reduced resistance, and perhaps faster Li^+ diffusion.

3.5. Magnetic properties of stoichiometric $LiMn_yNi_yCo_{1-2y}O_2$ ($y = 0.5, 0.4, 0.33$)

Determination of the magnetic behavior of these layered transition metal oxides can give us information both about the oxidation states and location of the transition metal ions in the crystal lattice. The temperature dependences of the magnetic susceptibility of $LiMn_yNi_yCo_{1-2y}O_2$ ($y = 0.5$, 0.4, 0.33) indicate Curie–Weiss behavior for all the compounds above 100 K (Fig. 7(a)). The values of the effective magnetic moment per transition metal ion μ and the Curie–Weiss temperatures Θ obtained from the fit of the high-temperature data to the Curie–Weiss law $\chi = N\mu^2/3k_B(T - \Theta)$ (see the straight lines in Fig. 7(a)) are presented in Table 4. The values of μ are in good agreement with those calculated assuming Mn^{4+} (spin $S = 3/2$, $\mu = 3.87\mu_B$), Ni^{2+} ($S = 1$, $\mu = 2.83\mu_B$), and low-spin Co^{3+} with zero magnetic moment (see Table 4). The Curie–Weiss temperatures are negative for all the compounds, indicating the antiferromagnetic character of the main magnetic interactions. With increasing Co content, the effective magnetic moment μ and the absolute value of the Curie–Weiss temperature both decrease as a result of dilution with non-magnetic Co^{3+} ions. At lower temperatures, a rapid increase of the magnetic susceptibility occurs. For $y = 0.5$, the fastest increase determined as an inflection point,

Table 4
Magnetic properties of stoichiometric $LiMn_yNi_yCo_{1-2y}O_2$ ($y = 0.5$, 0.4, 0.33) and hydrofluoric acid leached $Li_xMn_yNi_yCo_{1-2y}O_2$ ($y = 0.5$, 0.4)

Compound	μ (μ_B)	$\mu_{calculated}$ (μ_B)	Θ (K)	T_{inf} (K)
$LiMn_{0.5}Ni_{0.5}O_2$	3.12	3.39	−68.6(4)	36
$Li_{0.94}Mn_{0.5}Ni_{0.5}O_2$	3.11	3.35	−66.5(1)	–
$LiMn_{0.4}Ni_{0.4}Co_{0.2}O_2$	2.91	3.03	−61.6(2)	14
$Li_{0.47}Mn_{0.4}Ni_{0.4}Co_{0.2}O_2$	2.34	2.59	−46.2(2)	–
$LiMn_{1/3}Ni_{1/3}Co_{1/3}O_2$	2.59	2.77	−40.7(1)	8

$d^2\chi/dT^2 = 0$, is observed at $T_{inf} = 36$ K; at 15 K the susceptibility attains its maximum, $\chi = 0.23$ emu mol^{-1}, and then slightly decreases. In the Co-containing compounds the increase of susceptibility is less pronounced, a trend to saturation is observed instead of a maximum, and T_{inf} shifts to lower temperatures with increasing Co content (Table 4).

The magnetization curves of the Co-containing compounds also differ significantly from that of $LiMn_{0.5}Ni_{0.5}O_2$ (Fig. 7(b)). For $y = 1/3$, the magnetization curve in low fields is close to linear, there is minimal hysteresis; for $y = 0.4$ a small hysteresis is observed with a remanent magnetization $M_r \approx 4$ emu mol^{-1} and a coercive field $H_c \approx 70$ Oe; for $LiNi_{0.5}Mn_{0.5}O_2$ the hysteresis loop is significantly larger with $M_r \approx 140$ emu mol^{-1} and $H_c \approx 1100$ Oe. All compounds show no saturation of magnetization in the highest investigated field of 5 T, which is consistent with a domination of antiferromagnetic exchange. Thus, the variation of the Co content has a pronounced effect on the magnetic properties of the $LiMn_yNi_yCo_{1-2y}O_2$ materials. The role of cobalt ions in this effect is twofold: first, the increase of Co content leads to a dilution of the magnetic transition-metal layers with non-magnetic Co^{3+} ions; and second, cobalt is known to reduce the migration of Ni ions to the lithium sites, which leads to a better separation of the magnetic layers by reducing the number of the exchange pathways introduced by magnetic Ni ions between the layers. Therefore, the $LiMn_{1/3}Ni_{1/3}Co_{1/3}O_2$ compound exhibits mostly paramagnetic behavior with prevailing antiferromagnetic exchange. In $LiMn_{0.4}Ni_{0.4}Co_{0.2}O_2$, the signs of ferrimagnetic behavior appear, as evidenced by the small hysteresis of magnetization. The overall magnetic behavior of this compound is not much different from the previous one, but the increased Ni content on the Li sites leads to the formation of ferrimagnetic clusters that may include several magnetic ions in two different transition metal layers and the Ni ion on the Li site between them [53–57]. These clusters have a net magnetic moment leading to the ferromagnetic-like properties. In $LiNi_{0.5}Mn_{0.5}O_2$ the ferrimagnetic behavior becomes dominating as follows from the strong increase of the susceptibility and large hysteresis loop resulting from the formation of the net magnetic moment. However, the absence of magnetization saturation and the negative Θ imply mostly antiferromagnetic exchange, which indicates that atleast one of Mn^{4+}–Mn^{4+} (d^3–d^3), Ni^{2+}–Ni^{2+} (d^8–d^8), Mn^{4+}–Ni^{2+} (d^3–d^8) interactions is antiferromagnetic. The Goodenough–Kanamori–Anderson rules [58–60] predict ferromagnetic 90° d^3–d^3 superexchange experimentally found in Li_2MnO_3, ferromagnetic d^8–d^8 and antiferromagnetic d^3–d^8 superexchanges. These predictions should not be taken as granted for $LiMn_yNi_yCo_{1-2y}O_2$ compounds because they are derived considering relative strength of several superexchange mechanisms sensitive to the M–O bond length and the neighbors of intervening oxygen ligands to the extent that the exchange sign may become opposite [61].

3.6. Magnetic properties of lithium-rich $Li_{1+z}[Mn_{0.4}Ni_{0.4}Co_{0.2}]_{1-z}O_2$ ($0.9 < 1 + z < 1.25$)

A deficit or an excess of lithium changes both the oxidation states of the transition metals as well as the cation disorder in the layered structure as noted above, and therefore will influence their magnetic properties. The temperature dependences of the magnetic susceptibility of $Li_{1+z}[Mn_{0.4}Ni_{0.4}Co_{0.2}]_{1-z}O_2$ ($0.9 < 1 + z < 1.25$) are given in Fig. 8(a). The reciprocal magnetic susceptibility and representative fit of $1 + z = 0.9$ and 1.25 to the Curie–Weiss law (straight lines) at high temperatures are given in Fig. 8(b). Curie–Weiss behavior is observed for all compounds above 100 K except the most lithium deficient one of $1 + z = 0.9$, where linear behavior is observed only above 125 K. The values of the effective magnetic moment per transition metal ion μ and the Curie–Weiss temperatures Θ in $\chi = N\mu^2/3k_B(T - \Theta)$ are summarized in Table 5. The Curie–Weiss temperatures are negative for all the compounds, indicating the antiferromagnetic character of the main magnetic interactions. As the Li content increases, the effective magnetic moment μ and the absolute value of the Curie–Weiss temperature both decrease, suggesting the decrease of individual magnetic moment by changing of the oxidation state. The details of the calculation of the theoretical magnetic moment and the final calculated μ are given in Table 5. For the first two compounds with deficient lithium in Table 5, $Li_{0.94}M_{1.06}O_2$ and $Li_{0.96}M_{1.04}O_2$, where $M = Mn_{0.4}Ni_{0.4}Co_{0.2}$, the average oxidation state can be reduced by either a mixed valence of Mn^{4+}/Mn^{3+}, or Co^{3+}/Co^{2+}. The experimental increase of the magnetic moment relative to the stoichiometric compound is consistent with the reduction of Co^{3+} ($S = 0$) to Co^{2+} ($S = 1/2$, $\mu = 1.73\mu_B$); the reduction of Mn^{4+} ($S = 3/2$, $\mu = 3.87\mu_B$) to Mn^{3+} ($S = 2$, $\mu = 4.9\mu_B$) would result in a larger magnetic moment increase than that observed. For the lithium rich compounds the lower value of the measured magnetic moment than for the stoichiometric compound is consistent with a mixed valence of Ni^{2+}(spin $S = 1$, $\mu = 2.83\mu_B$)/Ni^{3+}(spin $S = 1/2$, $\mu = 1.73\mu_B$).

The magnetization versus magnetic field curves for $Li_{1+z}[Mn_{0.4}Ni_{0.4}Co_{0.2}]_{1-z}O_2$ where $0.9 < 1 + z < 1.25$ are shown in Fig. 8(c). There are significant differences between the lithium-rich and lithium-poor compounds, particularly at low fields. The lithium excess compounds show essentially linear behavior with minimal hysteresis loops. In contrast, $Li_{0.9}[Mn_{0.4}Ni_{0.4}Co_{0.2}]_{1.1}O_2$ has a significant hysteresis loop with a remanent magnetization $M_r \approx 180$ emu mol^{-1} and a coercive field $H_c \approx 600$ Oe. $Li_{0.97}[Mn_{0.4}Ni_{0.4}Co_{0.2}]_{1.03}O_2$ also exhibits a hysteresis loop but much smaller than that of $Li_{0.9}[Mn_{0.4}Ni_{0.4}Co_{0.2}]_{1.1}O_2$: $M_r \approx 40$ emu mol^{-1}, $H_c \approx 350$ Oe. All compounds show no saturation of magnetization in the highest investigated field of 5 T, which is consistent with a dominance of antiferromagnetic exchange. This magnetic behavior supports the hypothesis that an increased lithium content reduces the nickel content in the lithium layers.

3.7. Structural changes during lithium removal by electrochemical deintercalation

A series of samples with reduced lithium content were obtained by coulometric titration of the lithium from the stoichiometric $Li_xMn_{0.4}Ni_{0.4}Co_{0.2}O_2$, where $x = 1$, in an electrochemical cell; each composition required a separate experiment.

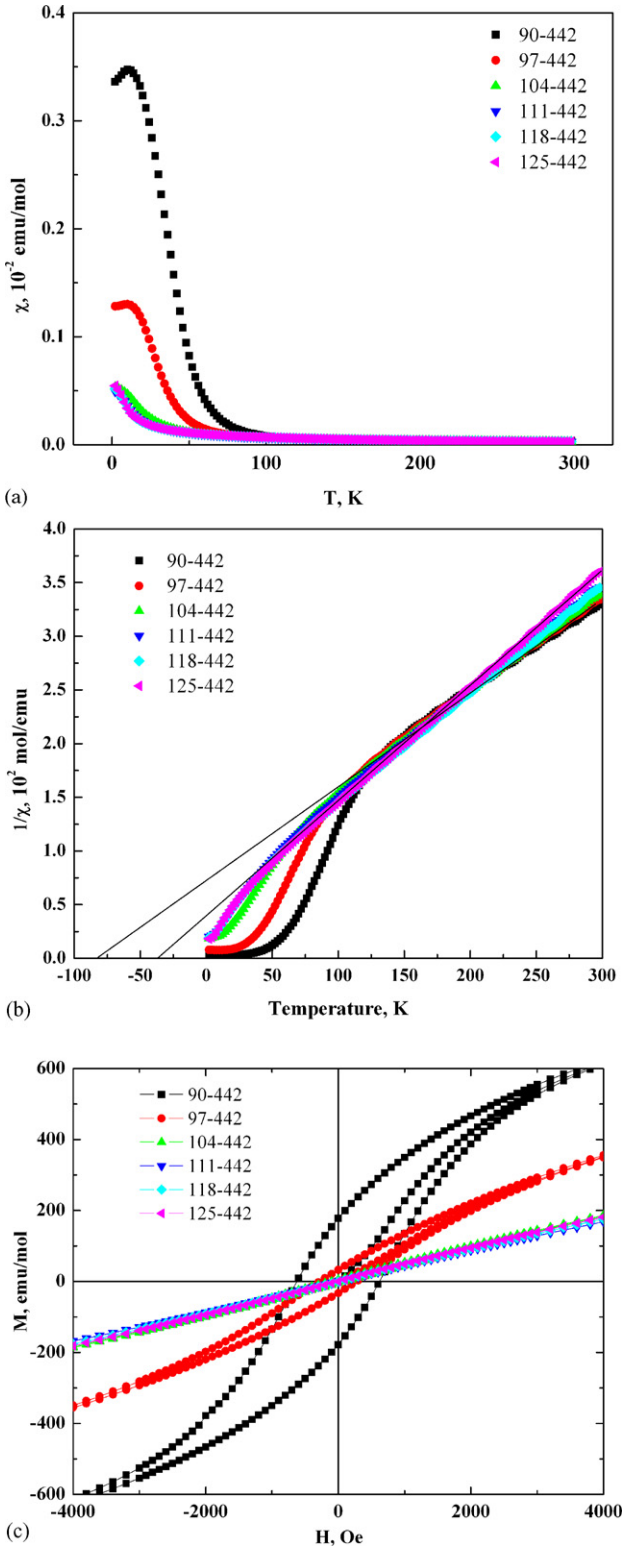

Fig. 8. Magnetic properties of $Li_{1+z}[Mn_{0.4}Ni_{0.4}Co_{0.2}]_{1-z}O_2$ ($0.9 < 1+z < 1.25$): (a) the temperature dependence of the magnetic susceptibility; (b) reciprocal magnetic susceptibility and representative fit of $z = 0.9$ and $z = 1.25$ to the Curie–Weiss law (straight lines) at high temperatures; (c) the comparison of the magnetization hysteresis loops vs. the magnetic field recorded at 5 K. The composition of the samples are given in the format, 100–442, where the first number represents the Li/M ratio × 100 and the second number the ratio of the transition metals; for 100–442 $LiMn_{0.4}Ni_{0.4}Co_{0.2}O_2$.

Table 5
Magnetic properties of $Li_{1+z}[Mn_{0.4}Ni_{0.4}Co_{0.2}]_{1-z}O_2$ ($0.9 < 1+z < 1.25$) and oxidation state of transition metals calculated from the linear fit of the reciprocal magnetic susceptibility

Initial ratio of Li/M	Actual Li/M ratio from DCP	Chemical formula $M = Mn_{0.402}Ni_{0.395}Co_{0.203}$	Θ (K)	μ (μ_B)	$\mu_{calculated}$ (μ_B)	Oxidation state of M	Possible cations	Amount and spin of mixed valence metal
0.90	0.884	$Li_{0.94}M_{1.06}O_2$	−103.2(3)	3.12	3.09	2.89	Mn^{4+}, Ni^{2+}, Co^{3+}/Co^{2+}	$0.11Co^{2+}$ ($S = 1/2$)
0.97	0.932	$Li_{0.96}M_{1.04}O_2$	−86.0(3)	3.03	3.07	2.92	Mn^{4+}, Ni^{2+}, Co^{3+}/Co^{2+}	$0.08Co^{2+}$ ($S = 1/2$)
1.04	1.026	$Li_{1.01}M_{0.99}O_2$	−68.5(2)	2.94	3.02	3.02	Mn^{4+}, Ni^{2+}/Ni^{3+}, Co^{3+}	$0.02Ni^{3+}$ ($S = 1/2$)
1.11	1.111	$Li_{1.05}M_{0.95}O_2$	−52.6(2)	2.85	2.94	3.11	Mn^{4+}, Ni^{2+}/Ni^{3+}, Co^{3+}	$0.11Ni^{3+}$ ($S = 1/2$)
1.18	1.193	$Li_{1.09}M_{0.91}O_2$	−45.7(2)	2.82	2.86	3.20	Mn^{4+}, Ni^{2+}/Ni^{3+}, Co^{3+}	$0.20Ni^{3+}$ ($S = 1/2$)
1.25	1.256	$Li_{1.12}M_{0.88}O_2$	−35.2(2)	2.72	2.80	3.27	Mn^{4+}, Ni^{2+}/Ni^{3+}, Co^{3+}	$0.27Ni^{3+}$ ($S = 1/2$)

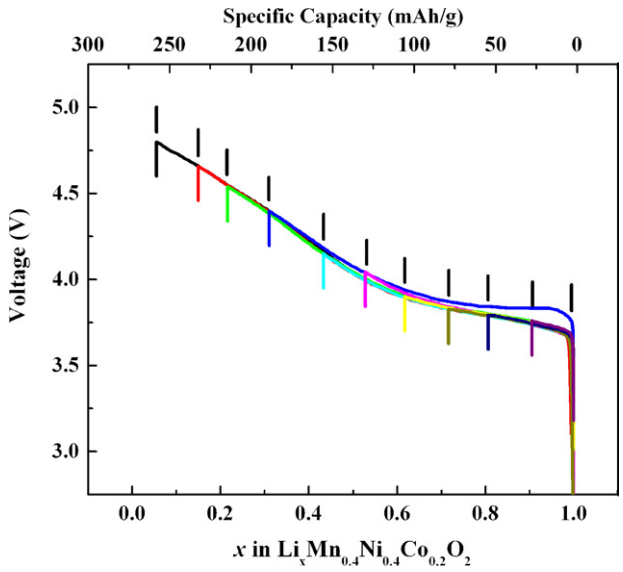

Fig. 9. First charge curves of deintercalated phases of $Li_xMn_{0.4}Ni_{0.4}Co_{0.2}O_2$ at 0.1 mA cm^{-2}.

The smooth charge curves shown in Fig. 9 suggest a single phase behavior of this compound unlike that observed for $LiCoO_2$. The reproducibility of the experiments can be observed by the superimposing of all the charge curves. The actual x-values were calculated by using the theoretical specific capacity of 278.6 mA h g^{-1}. The X-ray diffraction patterns are shown in Fig. 10(a), together with magnified views for the critical 2θ sections of 17–21° and 60–68° in Fig. 10(b). These two regions in Fig. 10(b) show the (0 0 3) reflection and the (1 0 8)/(1 1 0) reflections. The (0 0 3) reflection measures the interlayer spacing and shows an initial increase on lithium removal due to the increased interslab electrostatic repulsion of the oxygen layers. Eventually the separation decreases possibly due to an increasing covalent lattice. The separation of the (1 0 8)/(1 1 0) peaks shows an initial increase followed by a decrease, which indicates that the in-plane a-lattice parameter first decreases and then increases as the lithium content decreases; just the opposite of the c-lattice parameter. The refined lattice parameters are shown in Fig. 11 together with the cell volume as a function of the lithium content. The lattice parameters changes above $x = 0.4$ can be readily explained on bonding grounds. As the lithium content increases in this range, the positively charged lithium ions pull the MO_2 layers closer thus reducing the interlayer spacing; at the same time the electron density on the oxygen ions increases, thus increasing their effective ionic size and the a-lattice parameter, which is equal to the diameter of the oxygen ion in this close-packed lattice. The unit cell volume changes by only about 2.0% in the usual cycling regime of $x = 0.1$–0.9, which should lead to minimal grain breaking during cycling. At lithium contents below $x = 0.3$, the cell parameters were force-fitted to the hexagonal lattice and their absolute values have greater errors, but only at the lowest lithium content of $x = 0.05$ is there any trace of the one-block hexagonal close packed 1T structure; however, these hexagonal lattices may be distorted at low lithium contents leading to the line broadening. This is possibly a result of the nickel pinning, resulting in a metastable structure at low lithium contents. The $c/3a$ ratio of the hexagonal lattice increases from 1.658 for $x = 1.0$ to 1.712 for $x = 0.31$, then dropped to 1.664 as most of the lithium was removed. To confirm these structures, *in situ* synchrotron experiments were performed on $LiMn_{0.4}Ni_{0.4}Co_{0.2}O_2$ as well as on $LiMn_{1/3}Ni_{1/3}Co_{1/3}O_2$ cells as a comparison; they are consistent with the above data and will be published elsewhere [62]. We are also presently studying the above lattice changes after extensive cycling to see if there any permanent changes after the first cycle. In addition, we are determining the change in the interlayer spacing, that is the oxygen to oxygen distance across the lithium layer, as lithium is removed, as this spacing might impact the diffusion coefficient of the lithium.

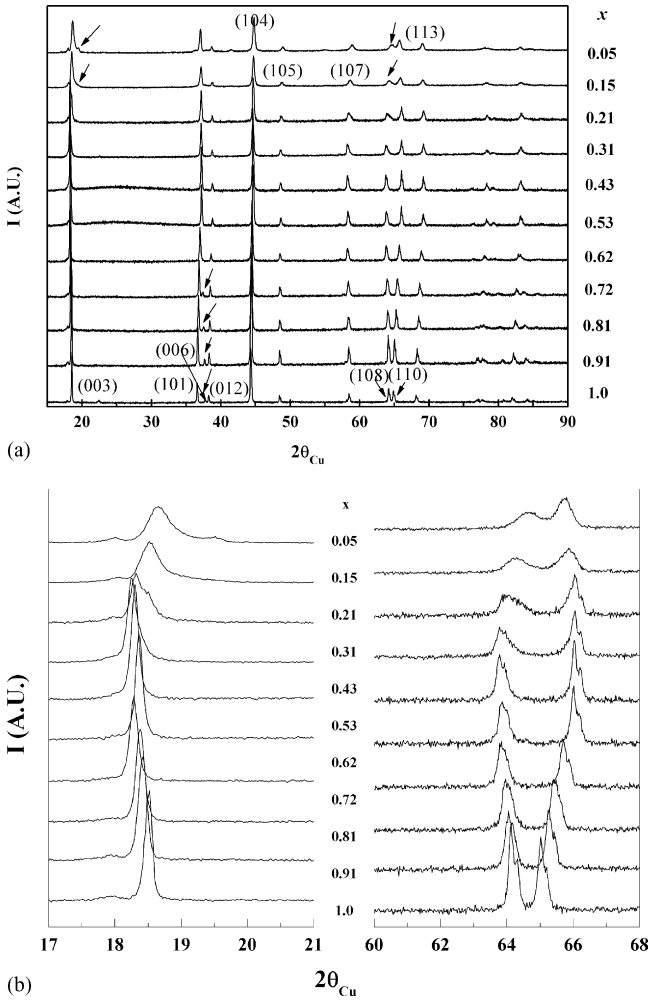

Fig. 10. X-ray diffraction patterns of the phase $Li_xMn_{0.4}Ni_{0.4}Co_{0.2}O_2$ as a function of lithium content: (a) full pattern, (b) 17–21° and 60–68° 2θ region. The cathode materials were removed from the electrochemical cells prior to X-ray analysis.

3.8. Chemical delithation of $LiMn_yNi_yCo_{1-2y}O_2$ by acid leaching

Hydrofluoric acid, HF, is formed if moisture is present in any of the battery components when using fluorine containing electrolyte salts, such as $LiPF_6$. This may cause the oxidation of the cathode material by an acid leaching effect. We studied the reactivity of a series of acids, including hydrofluoric

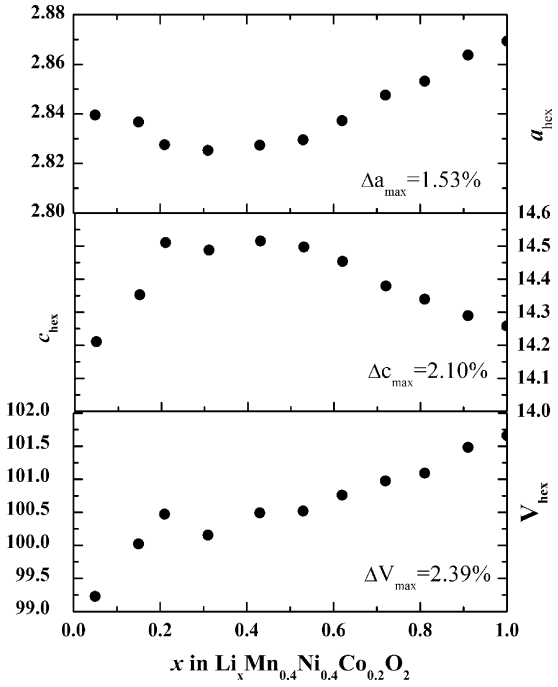

Fig. 11. Variation of (a) a_{hex}, (b) c_{hex}, and (c) V_{hex} vs. lithium content in $LiMn_{0.4}Ni_{0.4}Co_{0.2}O_2$ obtained from the electrochemical deintercalation.

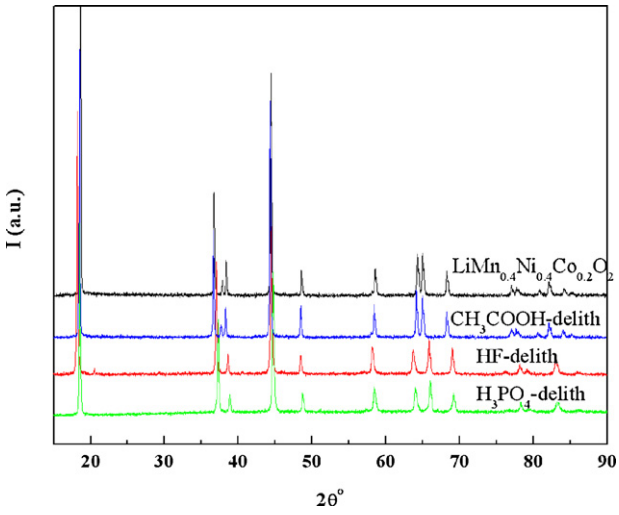

Fig. 12. XRD patterns of the original, acetic acid, hydrofluoric acid, and phosphoric acid leached $Li_xMn_{0.4}Ni_{0.4}Co_{0.2}O_2$ ($0<x<1$).

acid, to determine their leaching effect on the layered compound $LiMn_yNi_yCo_{1-2y}O_2$ ($y=0.33, 0.4, 0.5$). An added complication of these reactions is the possible exchange of lithium ions for protons.

The acid leached products $Li_xMn_{0.4}Ni_{0.4}Co_{0.2}O_2$ ($0<x<1$) had a range of lithium contents depending on acid and its strength. For 1.2 M solutions the degree of delithiation was in the order: acetic acid < hydrofluoric acid < phosphoric acid < hydrochloric acid < sulfuric acid. The solution was light pink, implying that a trace of the transition metal ions was leached into solution, as well as lithium ions. The XRD patterns of some chemical delithiated $Li_xMn_{0.4}Ni_{0.4}Co_{0.2}O_2$ ($0<x<1$) phases are shown in Fig. 12, along with that of the starting stoichiometric $LiMn_{0.4}Ni_{0.4}Co_{0.2}O_2$. Changes are clearly observable in the (0 0 3), (0 0 6), and (1 0 8)/(1 1 0) reflections, which are consistent with the loss of lithium ions, as described above. They are also consistent with hydrofluoric acid and phosphoric acid removing more lithium than the acetic acid.

The calculated cell parameter values from XRD, deduced lithium amount from XRD, and the actual chemical composition of cations from DCP measurements are shown in Table 6. All delithiated compounds had a smaller a and a larger c than the fully lithiated compound. This agrees with the trends of the cell parameter changes observed in the electrochemically deintercalated $Li_xMn_{0.4}Ni_{0.4}Co_{0.2}O_2$ for $0.4<x<1$, where a decreases and c increases (Fig. 11). Thus, for both the electrochemical and chemical deintercalation of lithium ions from this layered compound, the same trends of cell parameter changes were observed. From these observations, the unknown lithium value x can first be deduced by fitting the calculated cell parameters to the electrochemical deintercalation a and c curves (Fig. 11). Compared to the x value obtained from the DCP measurement, most deduced values were in good agreement with the actual values. As the strength of the acid increased, more lithium was deintercalated

Table 6
Chemical delithiation of $LiMn_yNi_yCo_{1-2y}O_2$ by acid leaching ($y=0.5, 0.4, 0.33$)

Samples	Acid (1.2 mol/l)	Cell parameters			x from XRD	DCP results				Cation mixing (%)
		a	c	$c/3a$		Li	Mn	Ni	Co	
$LiMn_{0.5}Ni_{0.5}O_2$	–	2.8761(4)	14.276(2)	1.655	1	1.06	0.495	0.505	–	7.29
$Li_xMn_{0.5}Ni_{0.5}O_2$	HF	2.8689(4)	14.293(2)	1.661	–	0.936	0.487	0.513	–	–
	HCl	2.8586(4)	14.324(2)	1.670	–	0.755	0.487	0.513	–	–
$LiMn_{0.4}Ni_{0.4}Co_{0.2}O_2$	–	2.8689(2)	14.267(1)	1.658	1	0.97	0.405	0.380	0.215	4.22
$Li_xMn_{0.4}Ni_{0.4}Co_{0.2}O_2$	CH_3COOH	2.86382(8)	14.2799(5)	1.662	0.9	0.893	0.404	0.380	0.216	–
	H_3PO_4	2.8321(3)	14.464(3)	1.702	0.57	0.558	0.401	0.383	0.216	–
	HF	2.8277(3)	14.489(3)	1.708	0.43	0.473	0.398	0.384	0.219	–
	HCl	2.8339(2)	14.426(1)	1.697	0.4	0.401	0.384	0.402	0.213	–
	H_2SO_4	2.8347(7)	14.391(5)	1.692	0.35	0.362	0.383	0.407	0.210	–
$LiMn_{1/3}Ni_{1/3}Co_{1/3}O_2$	–	2.8534(1)	14.2222(7)	1.661	1	1.03	0.325	0.33	0.345	1.45
$Li_xMn_{1/3}Ni_{1/3}Co_{1/3}O_2$	HF	–	–	–	–	0.512	0.319	0.332	0.349	–

from the layered structure. With the moderate concentration that had been used in this experiment (1.2 M), the maximum amount of lithium that can be deintercalated from the compound by the relatively strongest acid, which is sulfuric acid, was about 64%. For $LiNiO_2$, all the lithium could be removed when a high concentration of sulfuric acid was employed [63]. The DCP results showed that there had been minimal change, $\leq$1.4% in the transition metal ratio during the leaching.

The slight discrepancy between the lattice parameters in Fig. 11 and Table 6 is probably due to the ion exchange of a quantity of protons into the lattice, so that the effective oxidation state of the transition metals is lower than would be expected purely from the lithium content; this results in the lattice parameters being slightly different than expected. Only at low temperatures, such as 0 °C, as shown by Alcantara et al. [64] is proton ion-exchange minimized.

The SEM images of $LiMn_{0.4}Ni_{0.4}Co_{0.2}O_2$ before and after acid leaching by hydrofluoric acid, shown in Fig. 13, indicate no significant changes in the particle sizes. However, the agglomerated particles in the original compound were more broken down into their individual grains after leaching.

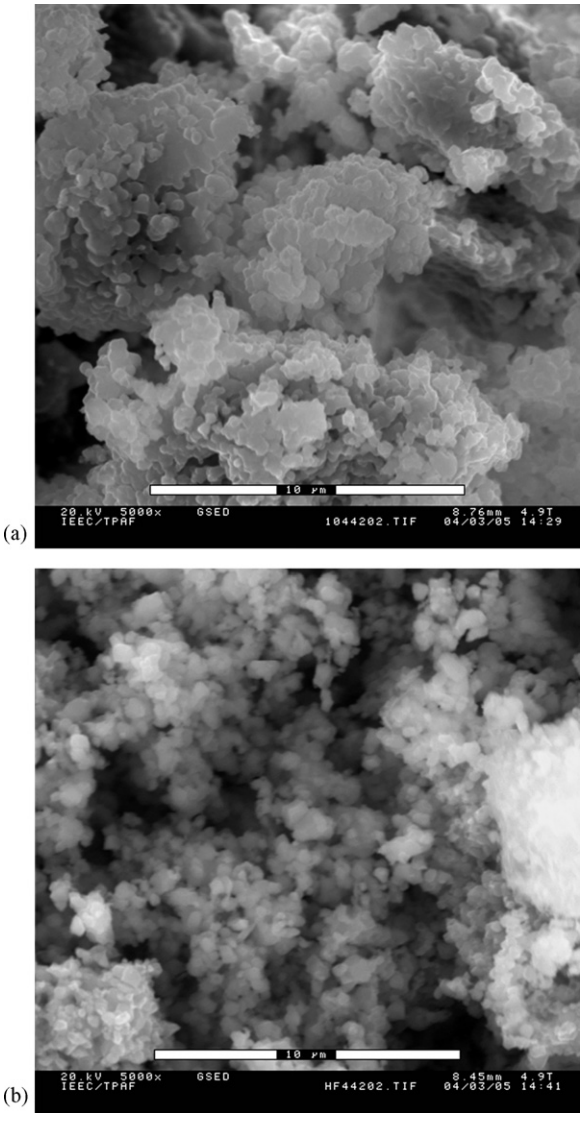

Fig. 13. SEM images of $LiMn_{0.4}Ni_{0.4}Co_{0.2}O_2$ before (a) and after (b) acid leaching for 5 h with hydrofluoric acid.

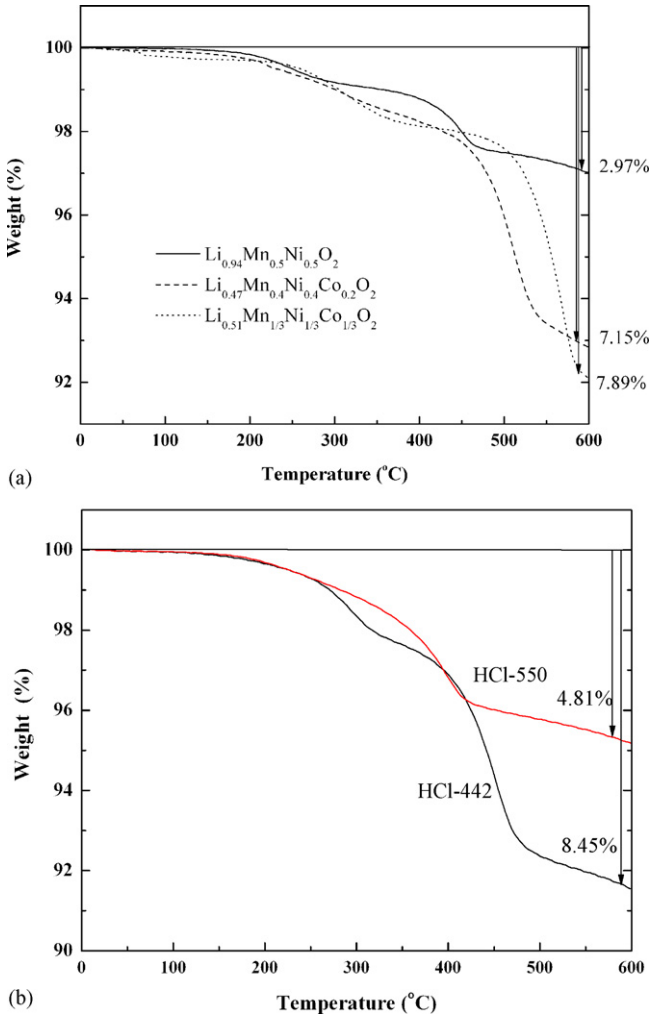

Fig. 14. TGA of (a) hydrofluoric acid delithiated $Li_xH_nMn_yNi_yCo_{1-2y}O_2$ (y = 0.33, 0.4, 0.5) and (b) hydrochloric acid delithiated $Li_xH_nMn_yNi_yCo_{1-2y}O_2$ (y = 0.4, 0.5) in nitrogen at 5 °C min^{-1} heating rate. The samples are identified by their transition metal content: 442 is $Li_xMn_{0.4}Ni_{0.4}Co_{0.2}O_2$, 550 is $Li_xMn_{0.5}Ni_{0.5}O_2$.

Table 6 also shows the effect of cobalt content on acid leaching using HF and HCl. For both acids, lithium deintercalation increases with increased cobalt content. Up to 50% of the lithium was deintercalated from the $LiMn_{1/3}Ni_{1/3}Co_{1/3}O_2$ compound and less than 10% from the cobalt-free compound after 5 h of acid leaching. This is possibly due to the increased lithium diffusion when the concentration of pinning nickel is decreased, as increasing cobalt reduces nickel disorder.

The thermal stability of these reduced lithium content compounds, $Li_xH_nMn_yNi_yCo_{1-2y}O_2$ (y = 0.33, 0.4, 0.5) is shown in Fig. 14(a) and (b) for the HF and HCl delithiated samples, respectively. Two weight loss plateaus were observed for all compounds. The first weight loss corresponds to the release of water associated with the hydrogen in the structure, and the second with the reduction of the transition metals and the related loss of oxygen [65]. Increasing the cobalt content raised the

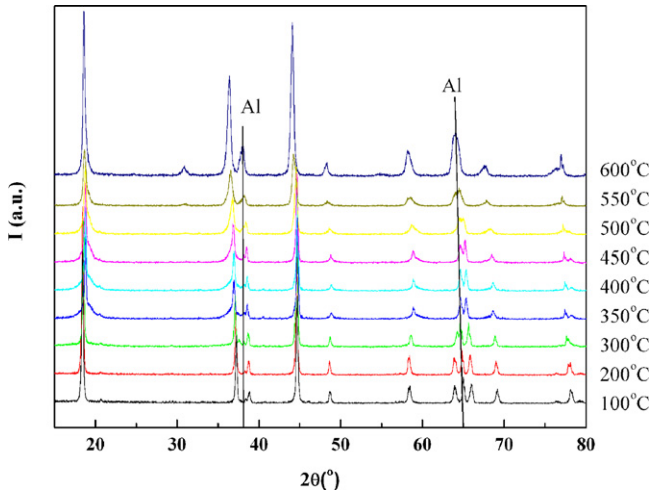

Fig. 15. *In situ* XRD patterns of HF delithiated $Li_xMn_{0.4}Ni_{0.4}Co_{0.2}O_2$ when heated in air to 600 °C.

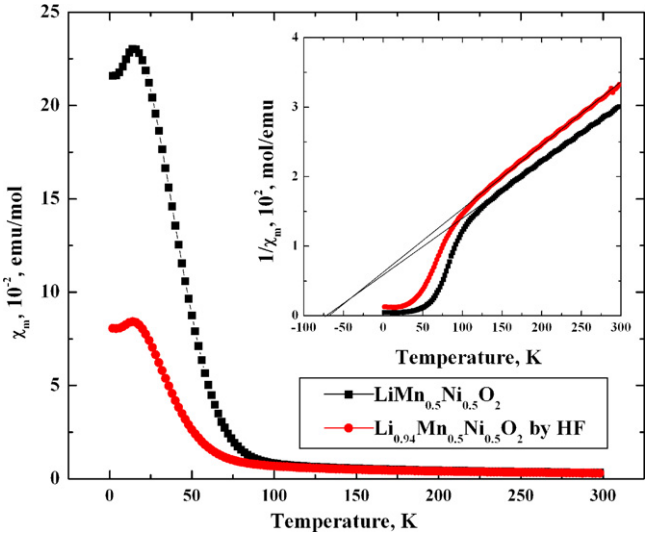

Fig. 16. Magnetic susceptibility of $Li_xMn_{0.5}Ni_{0.5}O_2$ reacted with HF and its reciprocal magnetic susceptibility with fit to the Curie–Weiss law (straight lines) at high temperatures.

temperature at which initial oxygen evolution is observed, even though the lithium content is lower. Thus, for the HF leached samples the beginning of oxygen loss is around 400, 450 °C and over 500 °C for cobalt contents of 0, 0.2 and 0.33, respectively, and where the lithium contents were 0.94, 0.47 and 0.51. Even though they had a lower lithium content, the cobalt containing compounds showed better thermal stability. This is similar to the behavior reported for the manganese free compounds [66]. In the case of the HCl leaching where more lithium is removed, $Li_{0.75}H_nMn_{0.5}Ni_{0.5}O_2$, and $Li_{0.4}H_nM_{0.4}Ni_{0.4}Co_{0.2}O_2$ the loss of oxygen begins at lower temperatures just as expected, but the same trends remain. Thus, the structural change from the layered starting material to a spinel-like product with the concomitant reduction of the Ni^{4+}/Ni^{3+} to Ni^{2+}, and some of the Mn^{4+} to Mn^{3+} is inhibited by the addition of cobalt. Depending on the precise structure and the oxygen partial pressure, Mn^{4+} can be stable to above 800 °C as for example in the compound $NiMnO_3H$ [67].

The thermal decomposition of the low lithium content mixed transition metal layered oxides leads initially to spinel-like structures. Fig. 15 shows the structural changes occurring when the HF delithiated $Li_xMn_{0.4}Ni_{0.4}Co_{0.2}O_2$ was heated in air on the X-ray stage. The broadening of the (0 0 3) reflection and the merging of the (1 0 8)/(1 1 0) reflections indicate that the change to a spinel-like structure started at 350 °C, corresponding to the first plateau on the TGA curve shown in Fig. 14(a). By 550 °C, the spinel structure was clearly characterized by the appearance of the (2 2 0) reflection around $2\theta = 31°$, as reflected in the second plateau on the TGA curve. Whether a disordered rock-salt structure was formed at the highest temperatures cannot be confirmed or dismissed, as those diffraction lines overlap with the spinel or aluminum holder lines.

The magnetic susceptibilities of the unreacted and the HF delithiated $Li_xMn_{0.5}Ni_{0.5}O_2$ are compared in Fig. 16. These results are consistent with the oxidation of Ni^{2+} to Ni^{3+} and Ni^{4+} on lithium removal. The experimental and calculated effective magnetic moment per transition metal ion μ, and the Curie–Weiss temperatures for $Li_xMn_yNi_yCo_{1-2y}O_2$ ($y = 0.4$, 0.5) before and after HF leaching are compared in Table 4. The calculated values of the effective magnetic moment are based on the assumption that the original oxidation states are Mn^{4+}, Ni^{2+}, and Co^{3+}, and the oxidation state after leaching are Mn^{4+}, a mixture of Ni^{2+} and Ni^{3+} for $Li_{0.94}Mn_{0.5}Ni_{0.5}O_2$, Mn^{4+}, Co^{3+}, a mixture of Ni^{3+} and Ni^{4+} for $Li_{0.47}Mn_{0.4}Ni_{0.4}Co_{0.2}O_2$. Thus, for $Li_{0.94}Mn_{0.5}Ni_{0.5}O_2$, it follows $\mu^2 = 0.5\mu^2_{Mn^{4+}} + 0.44\mu^2_{Ni^{2+}} + 0.06\mu^2_{Ni^{3+}}$ and $\mu = 3.35\mu_B$; $\mu = 2.59\mu_B$ for $Li_{0.47}Mn_{0.4}Ni_{0.4}Co_{0.2}O_2$. The antiferromagnetic character of the main magnetic interactions remained after leaching and with the oxidation of Ni^{2+} ($S = 1$, $\mu = 2.83\mu_B$) to Ni^{3+} ($S = 1/2$, $\mu = 1.73\mu_B$), or further to Ni^{4+} with no magnetic moment, the effective magnetic moment μ and the absolute value of the Curie–Weiss temperature both decreased.

3.9. *Electrochemistry of $LiMn_{0.4}Ni_{0.4}Co_{0.2}O_2$*

The electrochemical behavior of $LiMn_{0.4}Ni_{0.4}Co_{0.2}O_2$ was evaluated in both bag and button cells with lithium foil as the anode. We evaluated their discharge capacity, not only as a function of charge/discharge rate, but also as a function of charge cut-off voltage and temperature. Fig. 17(a) shows the charge/discharge curves as a function of current (0.1, 0.5, 1.0, 1.5, and 2.0 mA cm^{-2}) between 2.5 and 4.4 V at room temperature in bag cells; the charge and discharge rates were equal to each other. The initial open circuit voltage of the freshly assembled cells was around 3.2 V. On applying a constant current, the cell voltage rapidly increased to 3.7 V and then gradually increased until it reaches the top limit of 4.4 V for all current densities. The first-charge capacities fall between 180 and 200 mA h g^{-1}. The cell polarization and irreversible capacity increased as the current density increased. The irreversible capacity increases from 15 mA h g^{-1} for 0.1 mA cm^{-2} to 35 mA h g^{-1} for 2.0 mA cm^{-2}. The origin of this first cycle loss is not yet understood, but could be related to some irre-

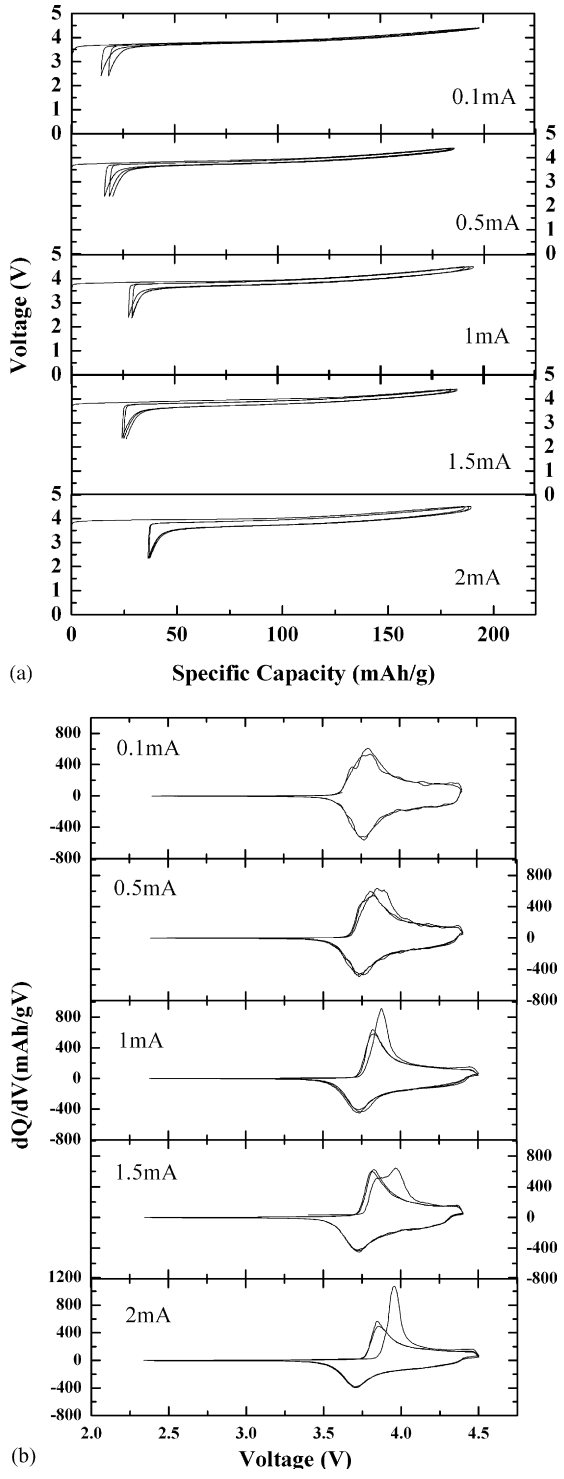

Fig. 17. (a) First three cycles of a Li/LiMn$_{0.4}$Ni$_{0.4}$Co$_{0.2}$O$_2$ bag cell at current densities of 0.1–2.0 mA cm^{-2} between 2.5 and 4.4 V and (b) the differential capacity vs. potential.

versible structural changes, such as cation migration, in addition to slow lithium in-diffusion for the last lithium insertion. The cycling curves obtained at 0.1 mA cm^{-2} are very close to the open circuit values, whereas the difference between the charge and discharge potentials increases to 0.3 V at a current density of 2.0 mA cm^{-2}. Fig. 17(b) shows the differential capacity versus potential over a range of current densities between 2.5 and 4.4 V. The peaks in dQ/dV correspond to the plateaus in the voltage profile of the charge and discharge curves in Fig. 17(a). A single peak is observed, with most of the capacity between 3.5 and 4.25 V, for both the charge and discharge process, indicative of the oxidation or reduction of the Ni^{2+}/Ni^{4+} redox couple. The first charge can be differentiated from the subsequent ones for all the curves except those cycled at 0.1 mA cm^{-2}. The difference between the first charge curve and the subsequent ones increases as the applied current density increased, indicating the increasing irreversibility. Besides, the potential difference ΔV between oxidation and reduction peaks also increases as the current density increased. Though the first charge capacities obtained at different current densities are close, difference in the irreversible capacity and polarization resulted in the difference of the first discharge capacity.

The first discharge capacity of bag cells over a range of current densities from 0.1 to 2.0 mA cm^{-2} between 2.5 and 4.4 V are shown in Fig. 18. These capacities range from about 150 to 180 mA h g^{-1}. The extended cycling of the cell at 1.5 mA cm^{-2} for the first 20 cycles is shown in Fig. 19. The first discharge capacity was 160 mA h g^{-1} with an irreversible capacity loss of 22 mA h g^{-1}, which corresponds to 0.08 lithium ions. This irreversible capacity appears in all the layered oxide compositions [33]. The capacity observed here is equivalent to cycling 70% of the nickel between Ni^{2+} and Ni^{4+}; the charging potential was insufficient to charge the cobalt. Subsequent charge and discharge capacities plot on top of each other, indicating small capacity loss and high efficiency during the following cycles. A higher capacity was obtained by charging the cell to a higher voltage or by topping up the charging by holding at 4.4 V.

The tests on the coin cells were performed at both 60 °C and room temperature. Fig. 20 shows the cyclic voltammogram at a sweep rate of 0.1 mV s^{-1}, and well-defined redox peaks are observed. The main oxidation peak is observed at 3.94 V after the first charge (all voltages mentioned are versus Li/Li$^+$) with a peak at 4.10 V only observed on the first charge, and the main

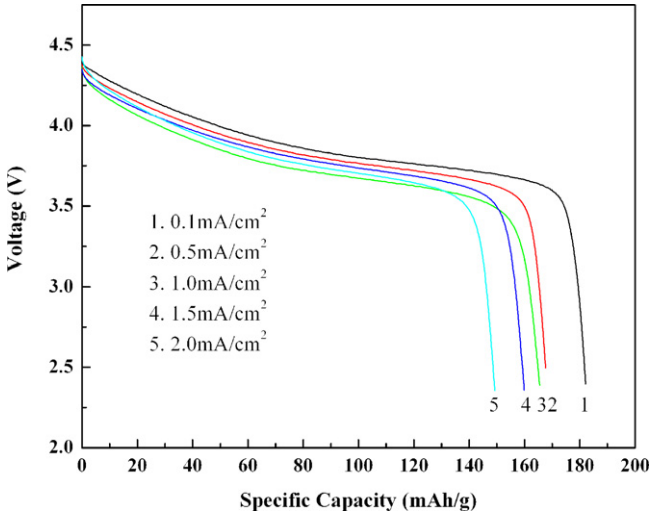

Fig. 18. The discharge capacity of a Li/LiMn$_{0.4}$Ni$_{0.4}$Co$_{0.2}$O$_2$ bag cell cycled at 0.1, 0.5, 1.0, 1.5, and 2.0 mA cm^{-2} between 2.5 and 4.4 V.

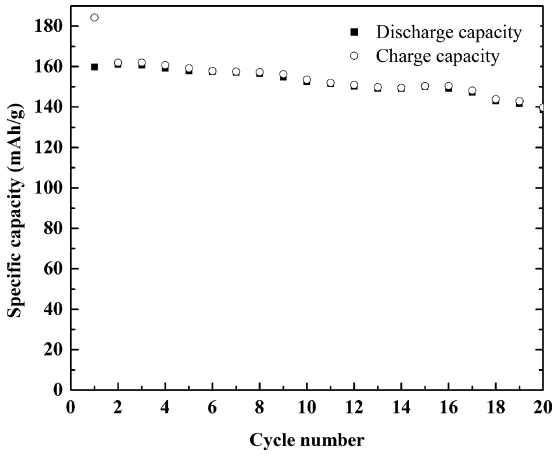

Fig. 19. The capacity for 20 cycles of a Li/$LiMn_{0.4}Ni_{0.4}Co_{0.2}O_2$ bag cell cycled at 1.5 mA cm^{-2} between 2.5 and 4.4 V.

reduction peak is located at 3.68 V. The 3.94 and 3.68 redox peaks are totally reproducible in subsequent cycles. The material shows a smaller ΔV (0.25 V) than $LiNi_{0.75}Co_{0.25}O_2$ (0.34 V) [68], which indicates that $LiMn_{0.4}Ni_{0.4}Co_{0.2}O_2$ has a smaller polarization than $LiNi_{0.75}Co_{0.25}O_2$. The lack of a peak around 3 V shows that the manganese in our synthesized materials is not in the 3+ oxidation state [69]. The loss of the 4.10 V peak after the first charge might be related to a change in structure associated with some reorganization of the nickel ions, or of side reactions such as SEI formation. No further changes in the voltammogram were observed after the first cycle, suggesting that all major changes occurred in that first charge.

The extended cycling of $LiMn_{0.4}Ni_{0.4}Co_{0.2}O_2$ in coin cells within the voltage range of 2.5–4.4 V at a constant current density of 0.12 mA cm^{-2} for a 100 cycles is shown in Fig. 21. This material demonstrates an excellent cyclability with an average capacity fading rate of 0.25 mA h g^{-1} per cycle. The initial capacity was 170 mA h g^{-1} and this stabilized out at 150 mA h g^{-1} after 40 cycles. Capacity was maintained at

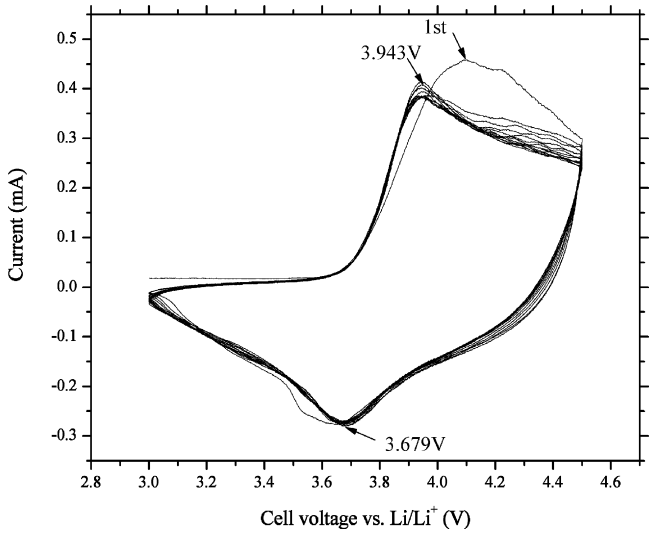

Fig. 20. Cyclic voltammetry of Li/$LiMn_{0.4}Ni_{0.4}Co_{0.2}O_2$ coin cell at a sweep rate of 0.1 mV s^{-1}.

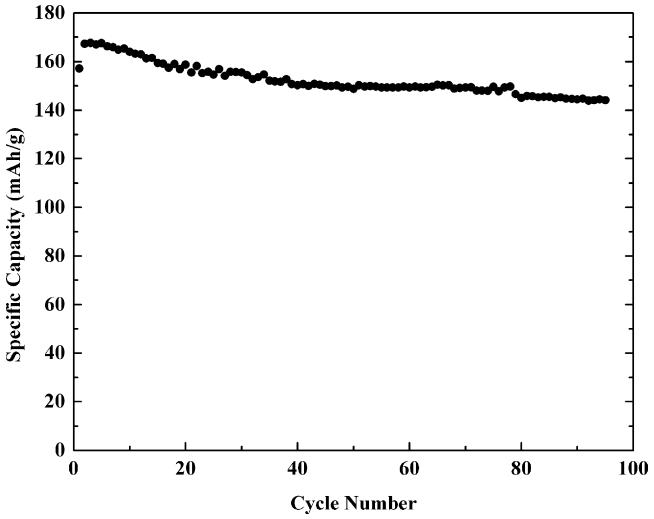

Fig. 21. The capacity over 100 cycles for a Li/$LiMn_{0.4}Ni_{0.4}Co_{0.2}O_2$ coin cell cycled at 0.12 mA cm^{-2} between 2.5 and 4.4 V.

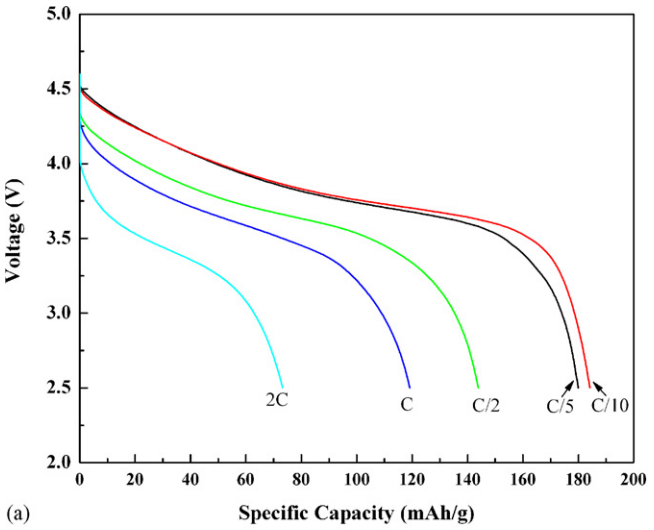

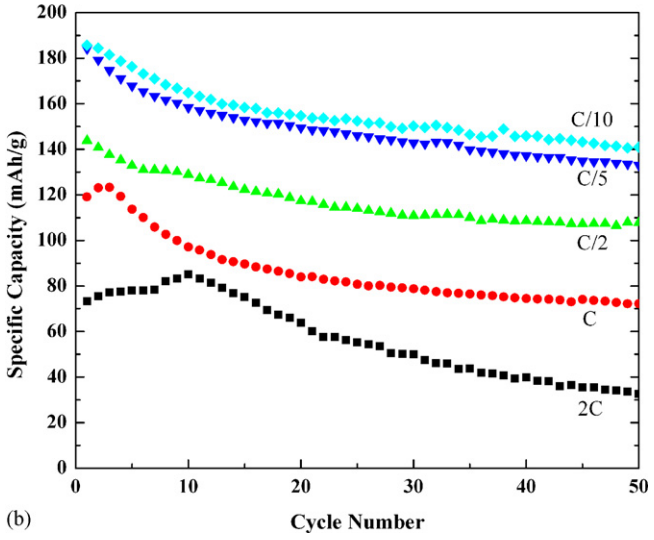

Fig. 22. (a) The first discharge capacities of Li/$LiMn_{0.4}Ni_{0.4}Co_{0.2}O_2$ coin cells cycled from 2.5 to 4.6 V at different C-rates and (b) the discharge capacity for 50 cycles.

150 mA h g^{-1} between 40 and 80 cycles and another capacity fading was observed after 80 cycles, with an overall capacity retention of 86%. A contributor to this capacity loss might well be the lithium foil which powders over such extended cycling, so that the actual capacity retention of the cathode could be well over 90%.

The rate capability of $LiMn_{0.4}Ni_{0.4}Co_{0.2}O_2$ in coin cells, cycled at C/10, C/5, C/2, C, and 2C between 2.5 and 4.6 V is shown in Fig. 22. The C-rate, for the cathode loadings of 8–10 mg cm^{-2} used here, is equivalent to 2.5 mA cm^{-2}. All cells were first subjected to one charge–discharge cycle at a C/10 rate between 2.5 and 4.6 V before switching to various C-rates in the subsequent cycles. Fig. 22(a) shows the initial discharge curves and Fig. 22(b) shows the discharge capacities for 50 cycles. The discharge capacity decreased with increasing C-rate as expected; at the 2C rate the electrode could only deliver a discharge capacity of 72 mA h g^{-1}, just 26% of the theoretical capacity and 39% of the C/10 capacity (184 mA h g^{-1}). The cell polarization also increased leading to a decreased average discharge potential with increasing cycling rate. With the same cut-off voltage of

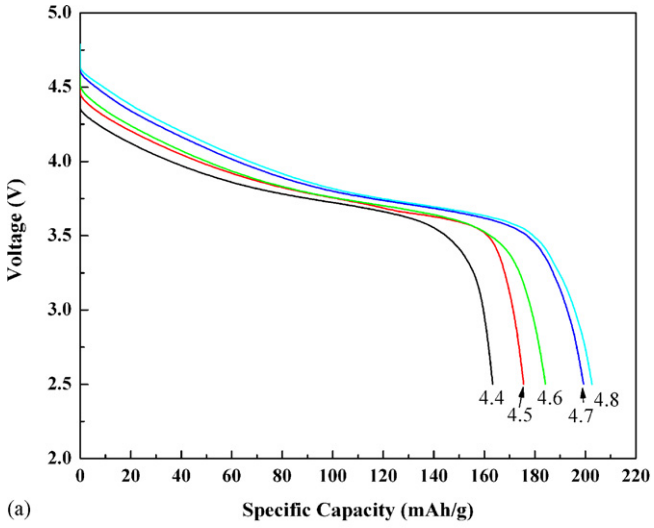

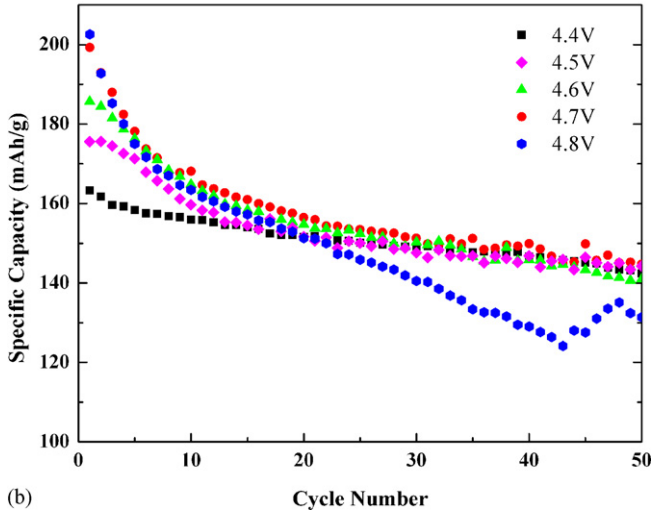

Fig. 23. (a) The first discharge capacities of $Li/LiMn_{0.4}Ni_{0.4}Co_{0.2}O_2$ coin cells cycled at C/10 with charge cut-off voltages of 2.5–4.4, 4.5, 4.6, 4.7, and 4.8 V and (b) the discharge capacity for 50 cycles.

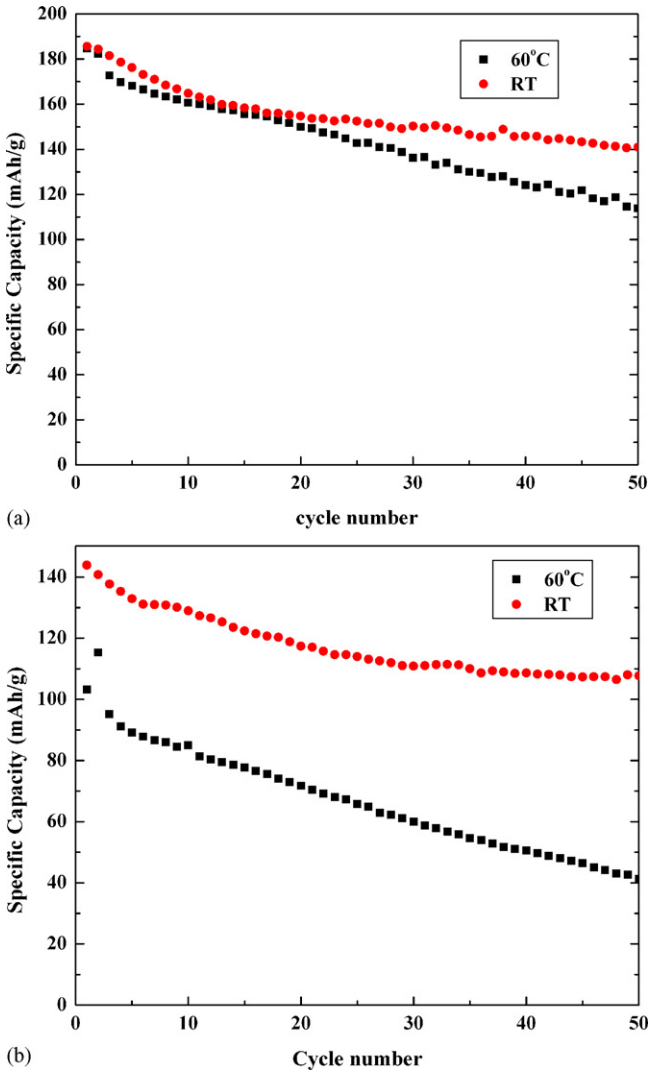

Fig. 24. Comparison of the cyclability of $Li/LiMn_{0.4}Ni_{0.4}Co_{0.2}O_2$ cells cycled at 60 °C and room temperature at (a) C/10 and (b) C/2 rate from 2.5 to 4.6 V.

2.5–4.6 V, capacity retention for 50 cycles are 72–76% for C/2 to C/10 rate, 60% for C rate, and 45.8% for 2C rate. The maximum discharge capacity for C and 2C rate cycling is observed on the third and the 10th cycle, respectively, which suggests some electrode changes are occurring such as particle decrepitation. The lower capacity obtained from C or 2C rate might also be related to applying the same rate for charging process, which is unfavorable for the lithium anode. Higher discharge capacity would be expected if a slower C/10 charging rate had been used.

The effect of changing the charge cut-off voltage was also investigated at a current density of 0.25 mA cm^{-2} (C/10 rate) is shown in Fig. 23 for voltage limits of 4.4, 4.5, 4.6, 4.7, and 4.8 V. Fig. 23(a) shows that the initial discharge capacities are 163.3, 175.6, 184.2, 199.3, and 202.6 mA h g^{-1} at cut-off voltages 4.4, 4.5, 4.6, 4.7, and 4.8 V, respectively; the higher cut-off voltage also gave a higher discharge plateaus. Fig. 23(b) shows that, even though a higher cut-off voltage gives higher capacities for the first 10 cycles, the discharge capacities fade faster at the higher cut-off voltages. The cell cycled within the smallest voltage window of 2.5–4.4 V showed the best capacity retention

of 87.7% after 50 cycles; in contrast, the 4.8 V cut-off voltage showed the poorest capacity retention with the capacity falling to 130 mA h g^{-1} after 50 cycles. This high capacity fade is almost certainly associated with the instability of the electrolyte used, $LiPF_6$ in EC/DMC, at these high potentials [70]. Thus, a cut-off voltage of around 4.4 V is probably optimum.

In large-scale applications, the cathode is likely to be subjected to elevated temperature operation. Thus, to evaluate the effect of temperature, coin cells were cycled at 60 °C at C/10 and C/2 rates between 2.5 and 4.6 V. Fig. 24(a) shows that cells cycled at a C/10 rate have the same capacities for the first 20 cycles when cycled at room temperature or 60 °C. However, beyond 20 cycles, the capacity retention is worse at 60 °C resulting in 25 mA h g^{-1} more capacity loss after 50 cycles. Even greater losses were observed at the C/2 rate, suggesting that resistive films were being formed from the decomposition of the electrolyte [71,72] at the elevated temperatures (Fig. 24(b)).

4. Conclusions

The layered compound $LiMn_{0.4}Ni_{0.4}Co_{0.2}O_2$ is a promising cathode material for lithium secondary batteries for large-scale application such as hybrid electric vehicles. $LiMn_{0.4}Ni_{0.4}Co_{0.2}O_2$ has a well-defined layered α-$NaFeO_2$ structure with the $R\bar{3}m$ space group. The Rietveld refinement of the X-ray data shows that 4.4(1)% nickel is in the lithium layer. $Li_xMn_{0.4}Ni_{0.4}Co_{0.2}O_2$ appears to be a single phase system for all values of x down to around 0.05, so that single phase behavior is expected within the normal cycling voltage ranges. Addition of excess lithium into the $Li_xMn_{0.4}Ni_{0.4}Co_{0.2}O_2$ phase reduces the particle size and thus gives a higher surface area. Magnetic measurements of the stoichiometric layered compounds $LiMn_yNi_yCo_{1-2y}O_2$ ($y = 0.33$, 0.4, 0.5) confirm that cobalt reduces the nickel content in the lithium layer. The nickel ions in the lithium layer minimize the formation of the 1T structure on lithium removal, so that the rhombohedral structure is maintained through cycling in contrast to $LiCoO_2$ and $LiMn_{0.33}Ni_{0.33}Co_{0.33}O_2$, thus enhancing capacity retention. The cell volume changes by less than 2% on cycling, minimizing the likely of particle decrepitation.

Acid treatment causes lithium loss from the layered compounds $LiMn_yNi_yCo_{1-2y}O_2$ ($y = 0.33$, 0.4, 0.5), and some protons are introduced. Cobalt enhances the lithium removal but provides better thermal stability to the leached product. Phase changes were observed upon heating of the delithiated layered compounds, which may lead to capacity loss of cells when in use. Magnetic studies of the delithiated compounds $Li_xMn_yNi_yCo_{1-2y}O_2$ ($y = 0.33$, 0.4, 0.5) showed that lithium removal was accompanied by the oxidation of Ni^{2+} ($S = 1$, $\mu = 2.83\mu_B$) to Ni^{3+} ($S = 1/2$, $\mu = 1.73\mu_B$).

Evaluation of the electrochemistry in both bag and coin cells showed that $LiMn_{0.4}Ni_{0.4}Co_{0.2}O_2$ has a discharge capacity of more than 180 mA h g^{-1} when the cell was cycled within a voltage window of 2.5–4.4 V at 0.1 mA cm^{-2}. The cyclability was reduced with increased currents, larger cut-off voltage windows, or elevated temperature.

Acknowledgements

We thank the US Department of Energy, Office of FreedomCAR and Vehicle Technologies, for their financial support through the BATT program at LBNL. We acknowledge the support of the National Institute of Standards and Technology, US Department of Commerce, in providing the neutron research facilities used in this work. This paper is based on the PhD thesis of M. Ma, and was part of the opening lecture presented at the Hawaii Battery Conference in Waikoloa, Hawaii on January 9, 2006. The rest of the lecture, which covered lithium iron phosphate, has been published separately [73].

References

[1] M.S. Whittingham, Science 192 (1976) 1126.
[2] M.S. Whittingham, US Patent 4,009,052 (1973).; M.S. Whittingham, UK Patent 1,468,416 (1973).
[3] K. Mitzushima, P.C. Jones, P.J. Wiseman, J.B. Goodenough, Mater. Res. Bull. 15 (1980) 783.
[4] J.B. Goodenough, K. Mizuchima, US Patent 4,302,518.
[5] Y. Nishi, in: M. Wakihara, O. Yamamoto (Eds.), Lithium Ion Batteries, Kodansha, Tokyo, 1998, p. 181.
[6] M. Broussely, Lithium Battery Discusssion, Bordeaux-Arcachon, 2001.
[7] E. Zhecheva, R. Stoyanova, Solid State Ionics 66 (1993) 143.
[8] A. Rougier, I. Saadouane, P. Gravereau, P. Willmann, C. Delmas, Solid State Ionics 90 (1996) 83.
[9] I. Saadoune, C. Delmas, J. Mater. Chem. 6 (1996) 193.
[10] A.R. Armstrong, P.G. Bruce, Nature 381 (1996) 499.
[11] F. Capitaine, P. Gravereau, C. Delmas, Solid State Ionics 89 (1996) 197.
[12] A.R. Armstrong, R. Gitzendanner, A.D. Robertson, P.G. Bruce, Chem. Commun. (1998).
[13] A.R. Armstrong, A.D. Robertson, P.G. Bruce, Electrochim. Acta 45 (1999) 285.
[14] A.R. Armstrong, A.J. Paterson, A.D. Robertson, P.G. Bruce, Chem. Mater. 14 (2002) 710.
[15] E. Rossen, C.D.W. Jones, J.R. Dahn, Solid State Ionics 57 (1992) 311.
[16] M.E. Spahr, P. Novák, B. Schnyder, O. Haas, R. Nesper, J. Electrochem. Soc. 145 (1998) 1113.
[17] Z. Liu, A. Yu, J.Y. Lee, J. Power Sources 81/82 (1999) 416.
[18] M. Yoshio, H. Noguchi, J. Itoh, M. Okada, T. Mouri, J. Power Sources 90 (2000) 176.
[19] T. Ohzuku, Y. Makimura, Chem. Lett. (2001) 642.
[20] Z. Lu, D.D. MacNeil, J.R. Dahn, Electrochem. Solid State Lett. 4 (2001) A200.
[21] T. Ohzuku, Y. Makimura, Chem. Lett. (2001) 744.
[22] Z. Lu, D.D. MacNeil, J.R. Dahn, Electrochem. Solid State Lett. 4 (2001) A191.
[23] Y. Makimura, T. Ohzuku, J. Power Sources 119–121 (2003) 156.
[24] Y. Sun, C. Ouyang, Z. Wang, X. Huang, L. Chen, J. Electrochem. Soc. 151 (2004) A504.
[25] S. Jouanneau, K.W. Eberman, L.J. Krause, J.R. Dahn, J. Electrochem. Soc. 150 (2003) A1637.
[26] D.D. MacNeil, Z. Lu, J.R. Dahn, J. Electrochem. Soc. 149 (2002) A1332.
[27] J.K. Ngala, N.A. Chernova, M. Ma, M. Mamak, P.Y. Zavalij, M.S. Whittingham, J. Mater. Chem. 14 (2004) 214.
[28] J.K. Ngala, N. Chernova, L. Matienzo, P.Y. Zavalij, M.S. Whittingham, Mater. Res. Soc. Symp. 756 (2003) 231.
[29] N. Yabuuchi, T. Ohzuku, J. Power Sources 119–121 (2003) 171.
[30] Y. Chen, G.X. Wang, K. Konstantinov, H.K. Liu, S.X. Dou, J. Power Sources 119–121 (2003) 184.
[31] Y.W. Tsai, J.F. Lee, D.G. Liu, B.J. Hwang, J. Mater. Chem. 14 (2004) 958.
[32] B.J. Hwang, Y.W. Tsai, C.H. Chen, R. Santhanam, J. Mater. Chem. 13 (2003) 1962.
[33] M.S. Whittingham, Chem. Rev. 104 (2004) 4271.

[34] W.S. Yoon, C.P. Grey, M. Balasubramanian, X.Q. Yang, D.A. Fischer, J. McBreen, Electrochem. Solid State Lett. 7 (2004) A53.
[35] Y. Koyama, I. tanaka, H. Adachi, Y. Makimura, T. Ohzuku, J. Power Sources 119–121 (2003) 644.
[36] I. Belharouak, Y.K. Sun, J. Liu, K. Amine, J. Power Sources 123 (2003) 247.
[37] D.C. Li, T. Muta, L.Q. Zhang, M. Yoshio, H. Noguchi, J. Power Sources 132 (2004) 150.
[38] B.H. Toby, J. Appl. Cryst. 34 (2001) 210.
[39] A.C. Larson, R.B. VonDreele, General Structure Analysis System (GSAS), Los Alamos National Laboratory Report LAUR, vol. 86, 2000, p. 748.
[40] Y.M. Todorov, K. Numata, Electrochim. Acta 50 (2004) 495.
[41] T. Horiba, K. Hironaka, T. Matsumura, T. Kai, M. Koseki, Y. Muranaka, J. Power Sources 119–121 (2003) 893.
[42] J. Cho, B. Park, J. Power Sources 92 (2001) 35.
[43] Z.L. Gong, H.S. Liu, X.J. Guo, Z.R. Zhang, Y. Yang, J. Power Sources 136 (2004) 139.
[44] S. Jouanneau, J.R. Dahn, Chem. Mater. 15 (2003) 495.
[45] Y. Song, P.Y. Zavalij, M.S. Whittingham, J. Electrochem. Soc. 152 (2005) A721.
[46] M. Guilmard, L. Croguennec, C. Delmas, Chem. Mater. 15 (2003) 4484.
[47] L. Zhang, H. Noguchi, M. Yoshio, J. Power Sources 110 (2002) 57.
[48] S.S. Shin, Y.K. Sun, K. Amine, J. Power Sources 112 (2002) 634.
[49] N. Tran, L. Croguennec, C. Jordy, P. Biensan, C. Delmas, Proceedings of the 12th International Meeting on Lithium Batteries, Nara, Japan, June, 2004, Abstract #314.
[50] S.T. Myung, S. Komaba, N. Kumagai, Solid State Ionics 170 (2004) 139.
[51] J. Choi, A. Manthiram, Electrochem. Solid State Lett. 8 (2005) C102.
[52] G.T.K. Fey, J.G. Chen, V. Subramanian, D.L. Huang, T. Akai, H. Masui, Mater. Chem. Phys. 79 (2003) 21.
[53] M. Guilmard, C. Pouillerie, L. Croguennec, C. Delmas, Solid State Ionics 160 (2003) 39.
[54] L. Croguennec, E. Suard, P. Willmann, C. Delmas, Chem. Mater. 14 (2002) 2149.
[55] D. Mertz, Y. Ksari, F. Celestini, J.M. Debierre, A. Stepanov, C. Delmas, Phys. Rev. B 61 (2000) 1240.
[56] A.L. Barra, G. Chouteau, A. Stepanov, A. Rougier, C. Delmas, Eur. Phys. J. B7 (1999) 551.
[57] M. Guilmard, A. Rougier, M. Grune, L. Croguennec, C. Delmas, J. Power Sources 115 (2003) 305.
[58] J.B. Goodenough, Magnetism and the Chemical Bond, Interscience, New York, 1963.
[59] J. Kanamori, J. Phys. Chem. Solids 10 (1959) 87.
[60] P.W. Anderson, Phys. Rev. 115 (1959) 2;
P.W. Anderson, Solid State Phys. 14 (1963) 99.
[61] W. Geertsma, D. Khomskii, Phys. Rev. B 54 (1996) 3011.
[62] W.S. Yoon, M. Ma, M.S. Whittingham, in preparation, 2006.
[63] H. Arai, Y. Sakurai, J. Power Sources 81 (1999) 401.
[64] R. Alcantara, J. Morales, J.L. Tirado, J. Electrochem. Soc. 142 (1995) 3997.
[65] M. Ma, N.A. Chernova, P.Y. Zavalij, M.S. Whittingham, Mater. Res. Soc. Proc. 835 (K11.3.1) (2005).
[66] K.K. Lee, W.S. Yoon, K.B. Kim, J. Electrochem. Soc. 148 (2001) A1164.
[67] R. Chen, P.Y. Zavalij, M.S. Whittingham, J. Mater. Chem. 9 (1999) 93.
[68] Y. Chen, G.X. Wang, J.P. Tian, K. Konstantinov, H.K. Liu, Electrochim. Acta 50 (2004) 435.
[69] J.M. Paulsen, C.L. Thomas, J.R. Dahn, J. Electrochem. Soc. 147 (2000) 861.
[70] A.G. Ritchie, J. Power Sources 136 (2004) 285.
[71] G. Nagasubramanian, J. Power Sources 119–121 (2003) 811.
[72] S.E. Sloop, J.B. Kerr, K. Kinoshita, J. Power Sources 119–121 (2003) 330.
[73] J. Chen, M.S. Whittingham, Electrochem. Commun. 8 (2006) 855.